Title

Insights into the mechanism and kinetics of propene oxidation and ammoxidation over bismuth molybdate catalysts derived from experiments and theory

Author

Bell, Alexis T

Publication Date

2022-04-01

DOI

10.1016/j.jcat.2021.05.009

Peer reviewed

Journal of Catalysis
Available online 19 May 2021
In Press, Corrected Proof

Insights into the mechanism and kinetics of propene oxidation and ammoxidation over bismuth molybdate catalysts derived from experiments and theory

Alexis T. Bell

Department of Chemical and Biomolecular Engineering, University of California, Berkeley, CA 94720, United States
Chemical Sciences Division, Lawrence Berkeley National Laboratory, Berkeley, CA 94720, United States

Received 8 February 2021, Revised 7 May 2021, Accepted 8 May 2021, Available online 19 May 2021.

https://doi.org/10.1016/j.jcat.2021.05.009

Highlights

- Propene oxidation and ammoxidation are both initiated by C—H bond activation.
- Mo=O bonds interacting with Bi cations are the active centers for C—H activation.
- Bi^{3+} cations adsorb both propene and ammonia for propene ammoxidation.
- Allyl amine is a critical intermediate in the formation of acrylonitrile.
- The activation energy for formation of allyl amine is lower than to acrolei

Abstract

Robert K. Grasselli was a pioneer in the development and commercialization of catalysts for propene oxidation to acrolein and ammoxidation to acrylonitrile, products that today are produced at the level of over 10 billion pounds per year. The catalysts used for both processes are contain bismuth molybdates augmented by up to seven additional elements used to attain high activity, selectivity, and stability. The importance of propene oxidation and ammoxidation has stimulated considerable interest in understanding the mechanism and kinetics of these processes and the particular role of catalyst composition and structure in defining catalyst activity and selectivity. Virtually all of this work has been carried out using bismuth molybdates, primarily α-$Bi_2Mo_3O_{12}$. The objective of this paper is to review the findings of experimental studies and illustrate how theoretical studies based on density functional theory provide additional insights that support deductions drawn from experiments and, more importantly, provide information that cannot be accessed experimentally.

Graphical abstract

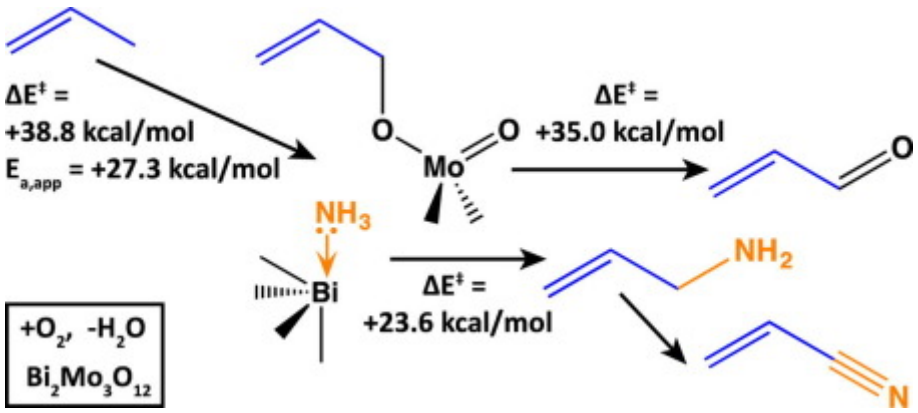

Download : Download high-res image (74KB) Download : Download full-size image

Keywords

Propene; Oxidation; Ammoxidation; Alpha-bismuth molybdate; Acrolein; Acrylonitrile

1. Introduction

FEEDBACK

The selective oxidation of hydrocarbons comprises a large fraction of the heterogeneous catalysts used for the production of chemical intermediates and final products. Amongst these, acrolein and acrylonitrile (reactions 1 and 2), produced by the oxidation and ammoxidation of propene, hold the top spots with each product being produced at about 10 billion pounds/year [1], [2], [3]. About 90% of acrolein is converted directly to acrylic acid, a key component of acrylic polymers, and more than half of the acrylonitrile produced is used to make acrylic fibers for textiles, with the remainder either polymerized to make plastics (ABS, SAN, NBR, etc.) or converted to acrylamide or adiponitrile. Two byproducts of propene ammoxidation, acetonitrile and hydrogen cyanide, also have commercial value. The catalysts used for both processes are based on bismuth molybdates developed in the late 1950s and first commercialized in the early 1960s [1]. While the industrial catalysts in use today contain up to seven elements in addition to Bi and Mo, which are added to enhance catalyst activity, selectivity, and stability, the core of the catalyst is still bismuth molybdate. Excellent summaries of the development of these catalysts and their evolution in activity and selectivity have been given by Robert Grasselli, who played a critical part in their discovery and development at SOHIO (later BP and INEOS) [4], [5].

$$CH_3CH = CH_2 + ½\ O_2 \rightarrow CH_2 = CHCHO + ½\ H \qquad 2O$$

$$CH_3CH = CH_2 + 3/2\ O_2 + NH_3 \rightarrow CH_2 = CHC{\equiv}N + 3\ H \qquad 2O$$

Given their commercial significance substantial effort has been devoted to understanding the mechanism and kinetics of propene oxidation and ammoxidation. Since industrial catalysts used for these process are complex and often contain multiple phases, virtually all of this work has been carried out with one of the unpromoted phases of bismuth molybdate, e.g., α-$Bi_2Mo_3O_{12}$, β-$Bi_2Mo_2O_9$, and γ-$BiMoO_6$. Experimental studies show that the β phase is marginally more active than the α phase and that the α and β phases are significantly more active than the γ phase [6], [7], [8]. Since the β phase is unstable in the absence of additives, most experimental and theoretical studies have focused on the α phase.

This paper presents a short overview the experimental evidence concerning the mechanism and kinetics of propene oxidation to acrolein and ammoxidation to acrylonitrile on α-$Bi_2Mo_3O_{12}$ and then discusses in more detail how theoretical studies based on density functional theory (DFT) have led to additional insights into the mechanisms of both reactions. A major part of the latter topic is based on studies reported by the author. Readers interested in a broader overview of propene oxidation are referred to the recent review by Grunwaldt and coworkers [9].

2. Experimental studies of propene oxidation and ammoxidation

Experimental investigations of propene oxidation over bismuth molybdate have focused on understanding the process by which propene is activated, the nature of the first intermediate formed, and whether the oxidant involved in propene oxidation derives from the catalyst or molecular O_2. Studies of propene oxidation over bismuth molybdate using deute

have demonstrated that the rate-limiting step is hydrogen abstraction from the methyl group of propene [10], [11], [12]. This step was originally thought to involve oxygen atoms associated with bismuth (e.g., Bi-O-Mo) [4], [5], [13], [14]; however, subsequent experimental and theoretical work strongly suggests that molybdenyl oxygen (i.e., Mo═O) atoms perturbed by a neighboring bismuth atom are the actuve sites for propene activation. Experiments conducted with ^{13}C labeled carbon have shown that this first step generates a symmetric, physisorbed π-allyl species [15], [16], [17]. This conclusion is supported by observations that allyl radicals generated *in-situ* on the catalyst surface are converted to acrolein [10], [11], [12], [18]. Studies conducted with gas-phase $^{18}O_2$ have shown that the O in the product acrolein comes from the catalyst surface via a Mars-van Krevelen mechanism [12], [19]. It has been hypothesized that acrolein is formed by addition of the allyl radical to a surface molybdenyl oxo (Mo═O) group to form a Mo-bound allyl alkoxide, which then undergoes hydrogen abstraction to produce acrolein [5]. The two abstracted hydrogen atoms are released as water during the reoxidation of the catalyst by molecular oxygen, thereby completing the overall reaction cycle. The catalyst elements that undergo reduction and oxidation has been a subject of discussion. While early work suggested the reduction of Bi^{3+} sites [5], more recent X-ray absorption studies have demonstrated that only Mo^{6+} undergoes reduction to Mo^{4+}, whereas Bi^{3+} is not reduced [20]a. Moreover, during steady-state propene oxidation, Mo is observed only in the 6+ state, indicating that the oxidation of Mo^{4+} is much more rapid than the reduction of Mo^{6+}.

The steady-state kinetics of propene oxidation over α-$Bi_2Mo_3O_{12}$, measured in the presence of at least a stoichiometric partial pressure of oxygen, are first order in propene and zero order in oxygen. Acrolein formation is generally observed to have an activation energy of ~20 kcal/mol, though values between 17 and 31 kcal/mol have been reported [5], [21], [22], [23], [24], [25]. The observation of zero order kinetics is fully consistent with the observation by X-ray absorption spectroscopy that the catalyst surface is fully oxidized under steady-state oxidation of propene [20]b.

Propene ammoxidation to acrylonitrile is more complex than propene oxidation and is accompanied by the formation of acetonitrile, hydrogen cyanide, propionitrile and N_2, in addition to CO_x, acrolein and H_2O. Nevertheless, several features of these two reactions are similar. The apparent activation energy for acrylonitrile formation is the same as for acrolein formation (~20 kcal/mol), as are the partial pressure dependencies (first order in propene pressure and zero order in oxygen, as long as ammonia and oxygen are supplied in at least stoichiometric quantities) [26], [27], [28]. Propene ammoxidation is also zero order in ammonia when the ratio of ammonia to propene partial pressures is greater than stoichiometric, suggesting the surface of the catalyst is saturated in adsorbed ammonia. As in the case of propene oxidation, ^{13}C labeling experiments indicate that the rate-limiting step for propene ammoxidation involves the initial abstraction of a hydrogen atom from the methyl group of propene, suggesting that propene activation occurs at the same catalyst surface sites for both reactions [10]. In the absence of gas-phase oxygen, the catalyst temporarily converts propene to acrylonitrile if ammon

indicating that activation of propene and subsequent hydrogen removal involves oxygen atoms that are part of the catalyst [29], [30].

The mechanism of propene ammoxidation following the initial activation of propene have been a subject of discussion, particularly the elementary step by which the C—N in acrylonitrile is formed. Grasselli et al. [5], [13] proposed that C—N bonds are formed by reaction of allyl species with surface Mo═NH groups. These latter species were envisioned as a product the reaction Mo = O + NH_3 → Mo = NH + H_2O. We note, though, that experimental evidence for Mo═NH groups on the surface of $Bi_2Mo_3O_{12}$ has not been reported and, as discussed below, theoretical calculations indicate that Mo═NH groups would be unstable under reaction conditions, since they will readily hydrolyze in the presence of water, a principal product of propene ammoxidation.

3. Theoretical studies of propene oxidation and ammoxidation

Theoretical studies based on DFT calculations have made it possible to test hypotheses proposed on the basis of experimental studies. Such investigations have been used to identify which species on the catalyst surface participate in the activation of propene and what are the subsequent elementary processes involved in the formation of acrolein and acrylonitirile. DFT calculations have also enabled exploration of how catalyst activity are selectivity are affected by catalyst composition and structure, and to ascertain why all catalysts used to promote propene and oxidation and ammoxidation involve Bi cations. We will begin an examination of these questions by summarizing the pioneering work of Goddard and coworkers conducted with small clusters of Mo and Bi oxides. This will be followed by a more detailed review our studies, which are based on periodic boundary DFT calculations for the (0 1 0) surface of $Bi_2Mo_3O_{12}$. The latter presentation also examinea the issue of what level of theory is required to achieve a physically realistic representation of the chemistry occurring on the catalyst surface.

3.1. Cluster calculations of propene oxidation and ammoxidation

The earliest effort to understand propene oxidation were reported by Goddard and co-workers [31], [32], [33]. The first of these studies appeared in 1985 and was based on small cluster of bismuth and molybdenum oxide and was carried out using GVB theory. High barriers were determined for propene activation on both bismuth (+3) oxide (41.6 kcal/mol) and molybdenum (+6) oxide (27.1 kcal/mol) clusters. Based on calculations conducted using a Mo_3O_9 cluster, Goddard and coworkers estimated that both the hydrogen abstraction step and the release of acrolein to leave a Mo^{4+} cation are demanding steps with activation barriers of 35.6 kcal/mol and 31.9 kcal/mol, respectively. The authors proposed that acrolein release may be facilitated by concurrent adsorption of gas phase oxygen on molybdenum, thereby maintaining molybdenum in a higher oxidation state and resulting in acrolein release being energetically favorable.

Goddard's group also investigated the mechanism of propene ammoxidation to acrylonitrile [33], [34], [35], [36], [37], [38]. These efforts focused largely on the reaction of allyl species with Mo═NH groups formed by the reaction of Mo═O groups in a Mo_3O_9 cluster with NH_3. While these investigations offer a plausible path to acrylonitrile, the stability of Mo═NH groups in the presence of water, a major byproduct of propene ammoxidation, needs to be considered. DFT calculations carried out on MoO_2Cl_2 clusters show that the Gibbs free energy of reaction at 673 K of $O{=}Mo^{6+}{=}O$ species and NH_3 to produce H_2O and $O{=}Mo^{6+}{=}NH$ species is + 12.4 kcal/mol, and that the formation of $HN = Mo^{6+} = NH$ species, suggested by Grasselli et al. [5] is even further uphill (+27.8 kcal/mol from the fully oxidized site) [34], [38]. Therefore, the very unfavorable thermodynamics for formation of Mo═NH groups suggests that in the presence of water, the surface concentration of Mo═NH groups should be very small. This conclusion is supported by the observed instability of Mo^{6+}=NR groups in organometallic complexes to hydrolytic decomposition in air at room temperature [39], [40], [41].

3.2. A model for the (0 1 0) surface of $Bi_2Mo_3O_{12}$

While theoretical studies conducted with small clusters of MoOx have provided important insights into the activation of propene, the first step in both propene oxidation to acrolein and ammoxidation to acrylonitrile, such structures are too small to capture the effects of Bi^{3+} cations on the properties of Mo═O groups at the surface of $Bi_2Mo_3O_{12}$ and the role of these cation in the elementary process involved in both reactions. To address these issues, we developed a more complete representation of the (0 1 0) surface of $Bi_2Mo_3O_{12}$ and evaluated the level of DFT required to achieve accurate estimates of the crystal lattice constants, the band gap, and the adsorption energies for propene and ammonia [42].

The (0 1 0) surface of $Bi_2Mo_3O_{12}$ was created by cleaving the $Bi_8Mo_{12}O_{48}$ unit cell along the crystallographic b-axis and introducing a vacuum space of 12 Å. The unit cell of $Bi_8Mo_{12}O_{48}$ was then decomposed into four $Bi_2Mo_3O_{12}$ layers stacked along the b axis. Of these, the top two layers were fully relaxed, while the bottom two layers were held fixed to their bulk positions. An illustration of the top-most layer is shown in Fig. 3 below. Periodic boundary DFT calculations were made in VASP using several different functionals in order to establish which functionals provide a physically meaningful representation of the catalyst and the energetics of propene oxidation and ammoxidation. The functionals considered were PBE [43], RPBE [43], [44], and M06-L [45], [46]. Hybrid DFT calculations were also carried out using the HSE functional [47], [48] and DFT + U calculations were carried out using the simplified, rotationally invariant formalism [44], [49]. Valence electrons were represented using a plane wave basis sets [50], while core electrons were modeled using projector augmented waves [51], [52] containing extra terms to allow calculation of the kinetic energy density contributions from core electrons [53]. The projector augmented wave cores used were designed for plane wave cutoff energies of 400 eV. Initial evaluation of the functionals for MoO_2 revealed that the relative computational burden to calculate the lattice parameters for MoO_2 using these functionals rose from 1.0 for RPBE to 2.7 for

RPBE + U(8.6 eV) to 9.7 for M06-L to 3,248 for HSE. As a consequence, calculations using the HSE functional were not pursued further.

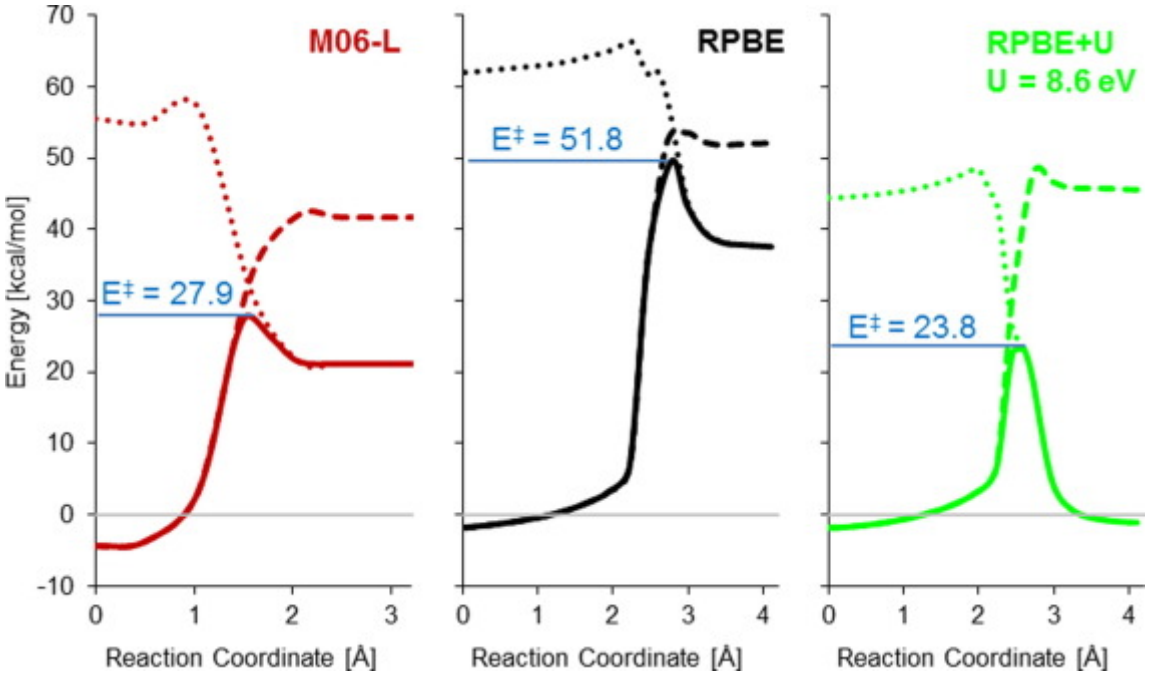

Download : Download high-res image (188KB) Download : Download full-size image

Fig. 1. Activation barriers for hydrogen abstraction from propene over $Bi_2Mo_3O_{12}$ calculated using M06-L, RPBE, and RPBE + U (8.6 eV). The singlet spin states are indicated by long dashes, the triplet spin states by short dots, and the spin-coupled reaction paths by solid lines. The zero of energy (gray line) is set by the energy of the bare slab and gas phase propene taken separately. Reproduced with permission from Ref. 43 (J. Phys. Chem. C, 117 (2013) 25562–25578). Copyright (2013) American Chemical Society.

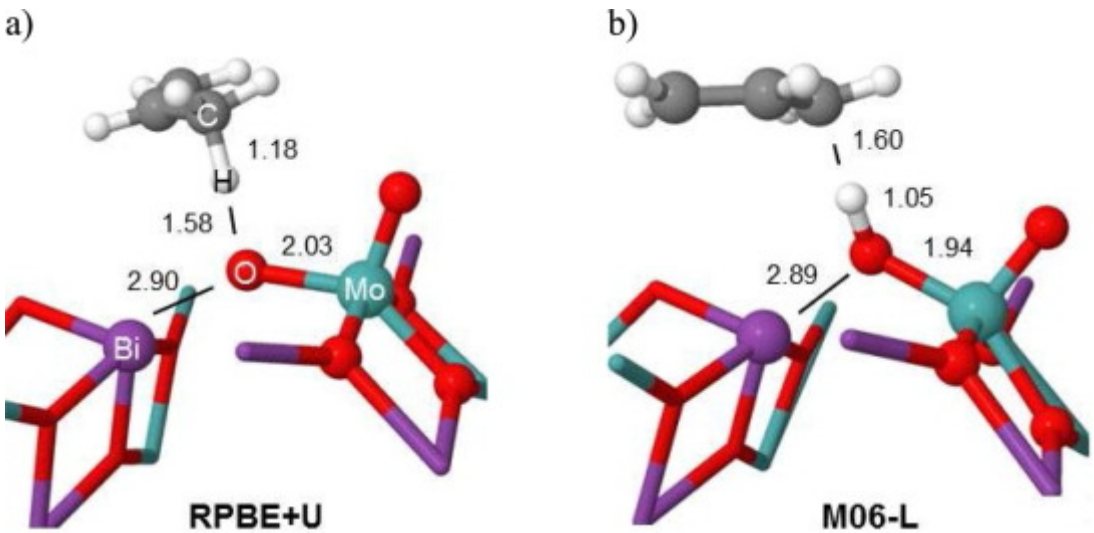

Fig. 2. Transition states for hydrogen abstraction from propene calculated using RPBE + U (U_{eff} = 8.6 eV) (a) and M06-L (b). Distances are in Å. For clarity, atoms in the catalyst surface not directly involved in the chemistry are not pictured. Reproduced with permission from Ref. 43 (J. Phys. Chem. C, 117 (2013) 25562–25578). Copyright (2013) American Chemical Society.

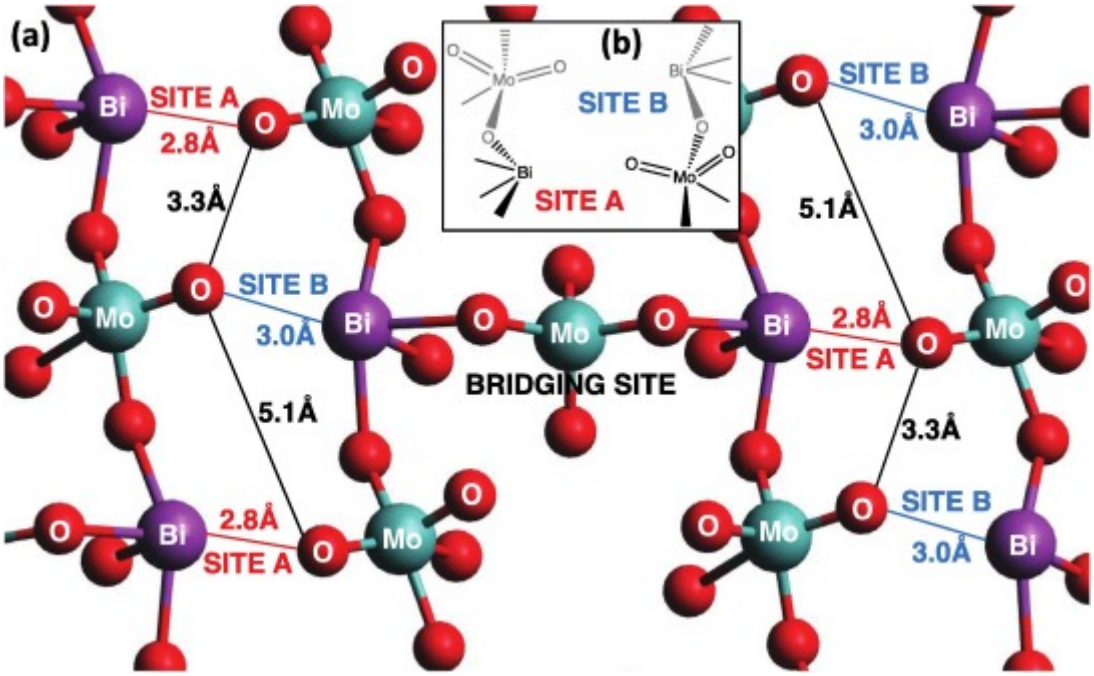

Fig. 3. (a) Top-down view of the top layer of optimized (0 1 0) surface of $Bi_2Mo_3O_{12}$, with relevant distances indicated in Å and the key **A** and **B** sites labeled. All red balls represent oxygen atoms, but only those marked with an "O" are at the surface. (b) Simplified representation of the same surface. Reproduced with permission from Ref. 56 (ACS Catal., 7 (2017) 161–176). Copyright (2017) American Chemical Society. (For interpretation of the references to colour in this figure legend, the reader is referred to the web version of this article.)

The performance of the RPBE + U and M06-L functionals for predicting the structural properties of $Bi_2Mo_3O_{12}$ is given in Table 1. The RPBE functional overestimates the lattice constants, particularly for the *b* lattice content. By contrast, the M06-L functional yields much better agreement with the experimentally determined lattice constants for $Bi_2Mo_3O_{12}$.

Table 1. Lattice constants for $Bi_2Mo_3O_{12}$ (Lengths in angstrom; volumes in cubic angstrom; U_{eff} = 8.6 eV). Reproduced with permission from Ref. 43 (J. Phys. Chem. C, 117 (2013) 25562–25578). Copyright (2013) American Chemical Society.

	Expt	RPBE + U	M06-L
a	7.7104	8.0186	7.7426
b	11.5313	12.2491	11.7374
c	11.972	12.308	12.065
β	115.276°	114.029°	116.057°
Vol	962.53	1103.75	984.99
		% ERROR	
a	–	4.00%	0.42%
b	–	6.22%	1.79%
c	–	2.81%	0.78%
Vol	–	11.47%	2.33%

The band gaps calculated for $Bi_2Mo_3O_{12}$ using RPBE + U and M06-L are given in Table 2. The RPBE functional significantly underestimates the band gap; however, increasing the value of U_{eff} increases the value of the estimated band gap, with the largest value tested, U_{eff} = 8.6 eV, actually leading to an over-estimation with respect to the experimental value. By contrast, the M06-L functional improves significantly on the RPBE functional, but still falls short of the experimental value.

Table 2. Band gaps for $Bi_2Mo_3O_{12}$. Reproduced with permission from Ref. 43 (J. Phys. Chem. C, 117 (2013) 25562–25578). Copyright (2013) American Chemical Society.

Functional	band gap (eV)
RPBE	2.55
RPBE + U (2.0 eV)	2.60

Functional	band gap (eV)
RPBE + U (4.0 eV)	2.70
RPBE + U (6.3 eV)	2.85
RPBE + U (8.6 eV)	3.05
M06-L	2.72
Experiment	2.95

The energetics involved in the initial activation of propene were calculated, as well, in order to further guide the choice of functional. Fig. 1 compares the reaction paths for the first hydrogen abstraction step determined from calculations carried out using the RPBE, RPBE + U(8.6 eV), and M06-L functionals. Zero in this figure is the sum of the energies of the bare catalyst surface and gas phase propene. The energy in each case starts below zero, reflecting physisorption of propene onto the catalyst surface. The M06-L physisorption energy is 4.4 kcal/mol, as compared to only 1.8 kcal/mol with RPBE(+U) and reflects the better ability of M06-L to capture the dispersive interactions responsible for physisorption. The experimental value for the heat of adsorption of propene is 7–8 kcal/mol [20], [24].

Following propene adsorption, the energy rises steeply and reaches a maximum at the transition state for hydrogen abstraction. This transition state occurs at the crossing between the spin-singlet and spin-triplet configurations of the system, a process for which the probability is highly favorable [42]. In the transition state as calculated using RPBE + U with U_{eff} = 8.6 eV, the singlet-triplet transition arises from a rehybridization of a closed shell Mo(+6) = O(–2) bond to form an Mo(+5)*—*O(–1) diradical. This bond breaking step is the rate-determining event in the RPBE + U calculations, and occurs prior to the hydrogen abstraction step. As shown in Fig. 2a, the C—H bond is only barely stretched from its initial length of 1.10 Å, while the O—H distance of 1.51 Å indicates that formation of the O—H bond has only just begun. The Mo—O bond distance at the transition state, however, is 2.03 Å, significantly longer than the value of 1.76 Å prior to reaction and nearly equal to its final length of 2.05 Å. This distance is characteristic of a Mo—O single bond.

As shown in Fig. 2b, when the calculation is conducted using the M06-L functional, a rather different picture of the transition state emerges. This functional predicts a Mo—O bond length of 1.94 Å in the transition state: stretched significantly from the initial value of 1.71 Å for the Mo ═O double bond, and near to the value of 2.00 Å for an Mo—O bond in the final state. Unlike the results obtained using RPBE + U, however, the C—H distance is stretched from 1.09 Å before reaction to 1.60 Å at the transition state, indicating that C—H bond dissociation is nearly complete when the transition state is reached. Conversely, the O—H distance is only 1.05 Å, close to its final value of 0.96 Å. Thus, the M06-L functional predicts that Mo═O bond

O—H bond formation, and C—H bond dissociation all occur in concert along the approach to the transition state, and that H atom transfer is nearly complete by the time the barrier energy is reached. A final difference between the transition states determined using the RPBE + U and M06-L functionals is visible in the orientation of the reacting propene molecule. The M06-L functional predicts stronger attractive interactions between propene and the catalyst, particularly with the bismuth atom adjacent to the active site. Thus, for the reaction pathway calculated using the M06-L functional, the propene molecule sits more squarely over the adjacent bismuth atom.

The M06-L functional predicts an intrinsic reaction barrier of 32.3 kcal/mol, which when combined with a calculated heat of adsorption of 4.4 kcal/mol leads to an apparent barrier of ~27.9 kcal/mol. This result is higher than the experimentally reported values of 17–21 kcal/mol, although about half of the difference results from the under-estimated heat of propene adsorption.

Also notable is the influence of the choice of functional on the energy of the final state. The effect of the + U_{eff} correction on the final state energy in RPBE + U calculations is similar to (actually slightly greater than) the effect on the barrier height; as a result, the energy of the final state is 17–24 kcal/mol lower than the highest energy along the reaction path for all values of U_{eff}. By contrast, the final state energy in the M06-L calculation is approximately 7 kcal/mol lower than the barrier energy. Since the final state produced by hydrogen abstraction involves a free allyl radical, it is reasonable that energy of this state should be relatively high. Thus, while the activation energy predicted by M06-L are higher than that obtained from experiment, the relative energy of the transition state versus the final state is chemically sensible.

The results presented in this section explain why all further calculations of the energetics involved in propene oxidation and ammoxidation were carried out using the M06-L functional. This functional provides reasonable geometries, electronic structures, and energies of reaction and does not involve a user-provided tuning parameter. It is also significant that the M06-L functional provides not only reasonable reaction barriers, but also reasonable heats of propene adsorption, as well as predicting correctly the energetic state of the final product of propene activation.

3.3. Mechanism of propene oxidation on the (0 1 0) surface of $Bi_2Mo_3O_{12}$

Our investigation of the mechanism and energetics of propene oxidation was conducted using the optimized slab model of $Bi_2Mo_3O_{12}$ described in the preceding section. Fig. 3 shows the fully relaxed (0 1 0) surface of this material [54]. Highlighted sites **A** and **B** are both oxygen atoms formally doubly bonded to molybdenum cations and electronically perturbed by neighboring bismuth cations. Preliminary studies showed that unperturbed Mo═O groups are less active than Bi-perturbed ones, and that bismuth-molybdenum bridging oxygen sites are even less active than either of the molybdenum oxos [55]. However, since site **A** is slightly closer to the nearby bismuth than site **B** (2.8 Å and 3.0 Å respectively) and is perturbed more strongly,

most active surface site and was used as the primary site for calculations involving the oxidation (and ammoxidation) of propene.

Scheme 1 shows the elementary steps for propene oxidation to acrolein and the corresponding energy profile is shown in Fig. 4. Two variants of the oxidation mechanism are shown corresponding to the absence or presence of ammonia adsorbed on a Bi^{3+} site. In agreement with experiment, the initial activation of propene to produce a physisorbed allyl radical (steps **0 → 3**) is rate-limiting and is common to both propene oxidation and ammoxidation. The subsequent steps (**3 → 8**) are very similar to those proposed previously [56], [56], [58].

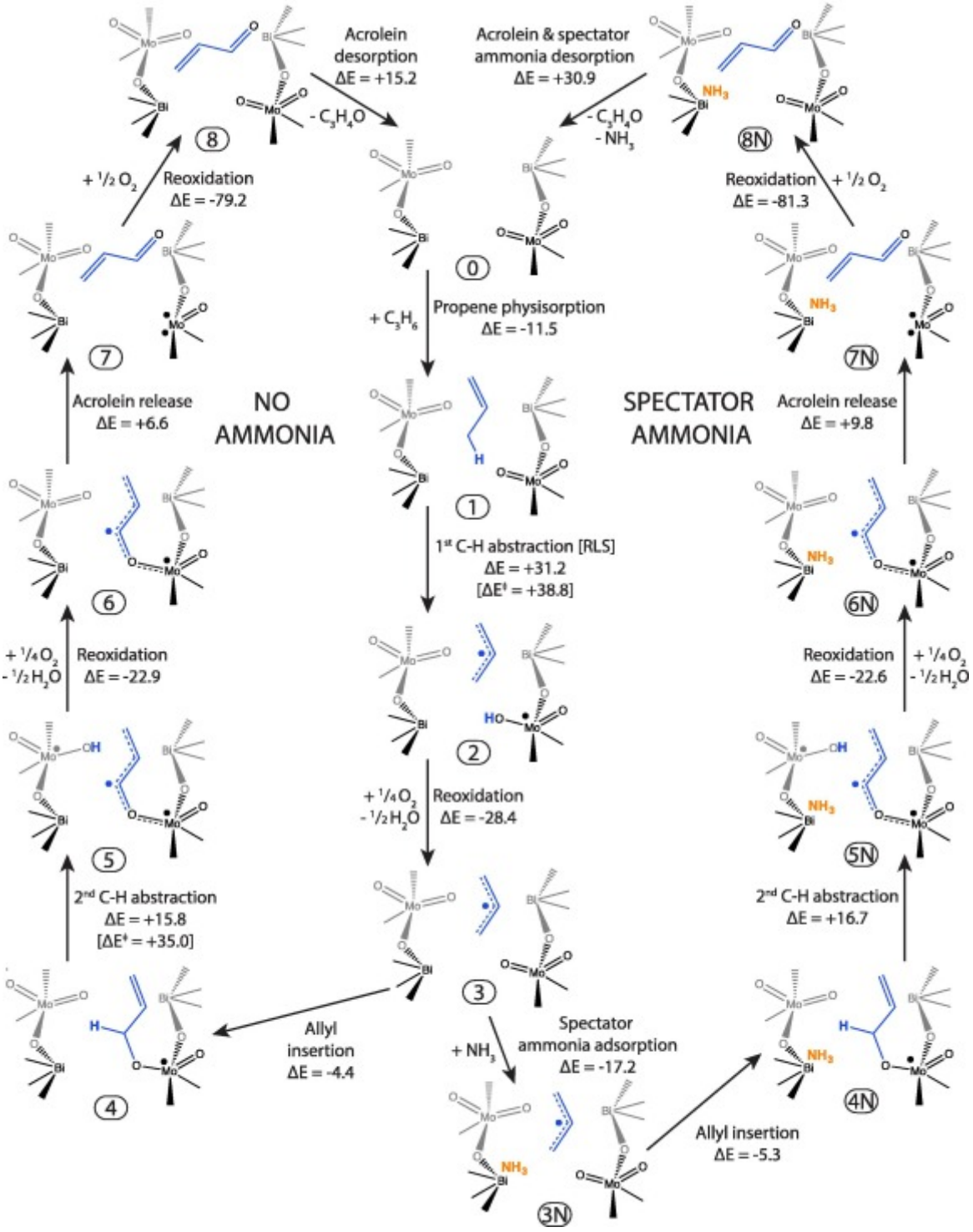

Download : Download high-res image (742KB) Download : Download full-size image

Scheme 1. Proposed elementary steps for propene oxidation to acrolein (ΔE in kcal/mol). Reproduced with permission from Ref. 56 (ACS Catal., 7 (2017) 161–176). Copyright (2017) American Chemical Society.

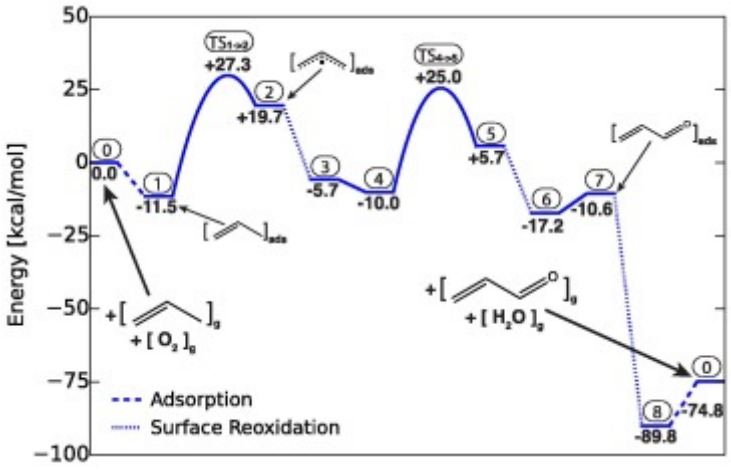

Download : Download high-res image (163KB) Download : Download full-size image

Fig. 4. Energy landscape for propene oxidation to acrolein. Encircled integers refer to structures in Scheme 1, bold numbers give the energy of each structure relative to the initial state. Reproduced with permission from Ref. 56 (ACS Catal., 7 (2017) 161–176). Copyright (2017) American Chemical Society.

The first step (**0 → 1**) represents propene physisorption. While we previously reported an internal energy of adsorption over the (0 1 0) surface of $Bi_2Mo_3O_{12}$ of –4.4 kcal/mol, corresponding to non-specific van der Waals adsorption above the space between sites **A** and **B** [42], subsequent investigation revealed that the strongest propene adsorption site is directly over a surface Bi^{3+} atom at a distance of 3.33 Å from the center of the double bond. In this adsorption mode, the pi-bonding electrons of propene donate electron density to the under-coordinated Bi^{3+} via a dative interaction, resulting in a calculated internal energy of adsorption of –11.5 kcal/mol. For comparison, the experimental value for the enthalpy of adsorption of propene on bismuth molybdate is ~8 kcal/mol [57].

The second step (**1 → 2**) involves abstraction of a hydrogen atom from the methyl group of propene by a bismuth-perturbed molybdenyl oxo and proceeds via a singlet-triplet spin crossing transition state, which is calculated to have a high probability of occurring [42], [56]. The reaction pathway starting from propene adsorbed over a neighboring Bi^{3+}, including the spin-singlet, spin-triplet and spin-coupled energy landscapes and geometries for the initial, spin crossing, and final state, is shown in Fig. 5. From its lowest energy adsorbed state, the propene moves parallel to the surface towards the molybdenyl oxo and passes over the hydrogen, then moves back to re-establish a dative interaction between the newly formed allyl radical and the bismuth cation. After subtracting the spin-orbit coupling energy from the spin-crossing point to attain the reaction pathway transition state, the value of ΔE_{TS} is found to be 38.9 kcal/mol. Since at reaction temperatures of ~673 K, the catalyst resting state is the bare catalyst surface, the p

adsorption energy is subtracted from the transition state energy to obtain an apparent activation energy of 27.3 kcal/mol.

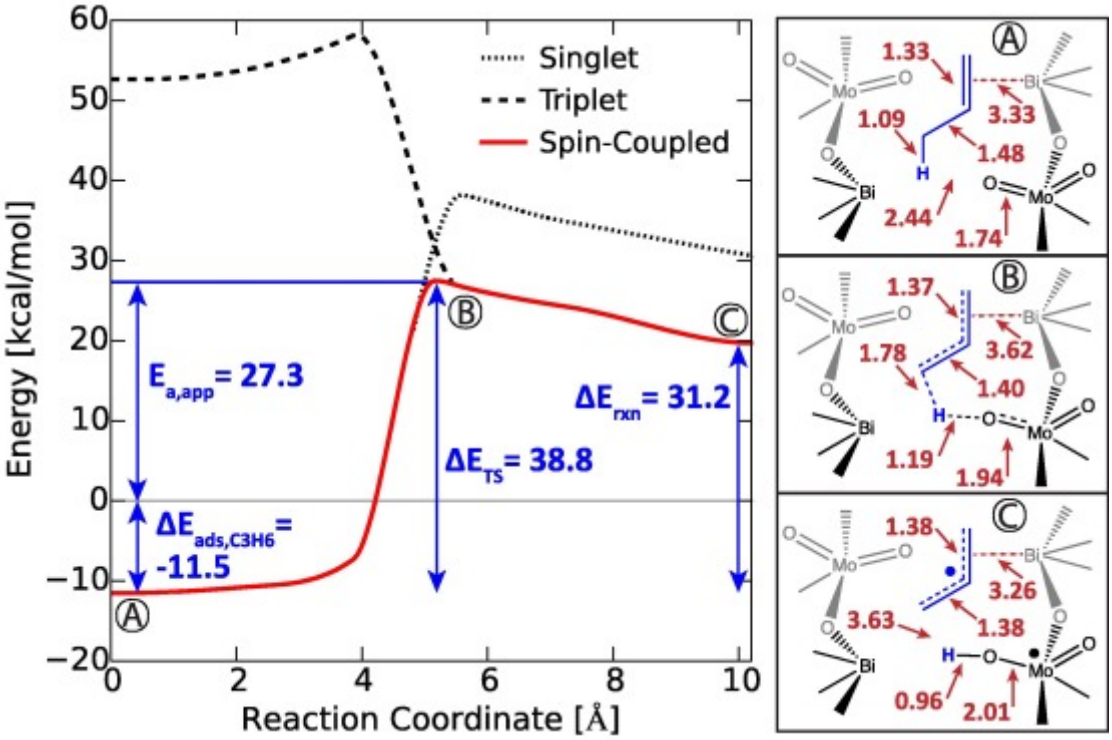

Download : Download high-res image (438KB) Download : Download full-size image

Fig. 5. Optimized spin-crossing reaction barrier for initial hydrogen abstraction from propene, with relevant energies annotated. Geometries for the initial state (A), spin-crossing transition state (B) and final state (C) are shown on the right, with relevant distances in Å indicated. Reproduced with permission from Ref. 56 (ACS Catal., 7 (2017) 161–176). Copyright (2017) American Chemical Society.

The overall energy of reaction, ΔE_{rxn}, is very similar to the value of ΔE_{TS}, since the final state contains a high-energy radical species. In fact, we can see from the geometries on the right-hand side of Fig. 5 that the transition-state geometry is very similar to the final-state geometry, with the molybdenum-oxygen bond highly elongated, the oxygen-hydrogen bond almost completely formed, the carbon-hydrogen bond already completely broken and the two carbon-carbon bonds of almost equal length. While it appears that this reaction could easily go backward via **2 → 1**, this is unlikely to occur because of rapid catalyst reoxidation. As is clear from Fig. 4, catalyst reoxidation removes the hydrogen atom and leave an allyl radical stabilized over an oxidized surface (**2 → 3**).

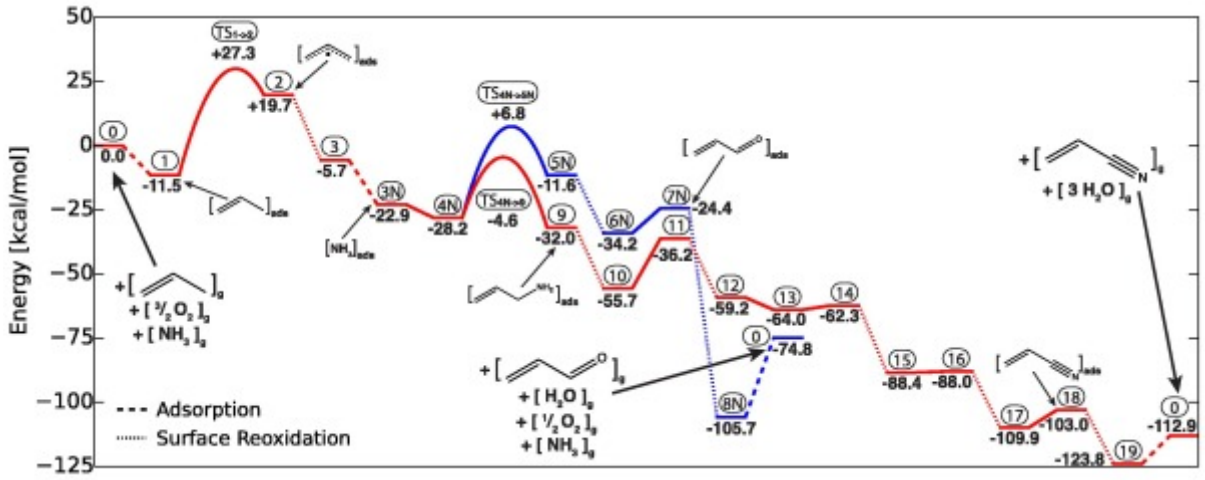

Download : Download high-res image (285KB) Download : Download full-size image

Fig. 6. Energy landscape for propene ammoxidation to acrylonitrile. Encircled integers refer to structures in Scheme 2, bold numbers give the energy of each structure relative to the initial state. Reproduced with permission from Ref. 56 (ACS Catal., 7 (2017) 161–176). Copyright (2017) American Chemical Society.

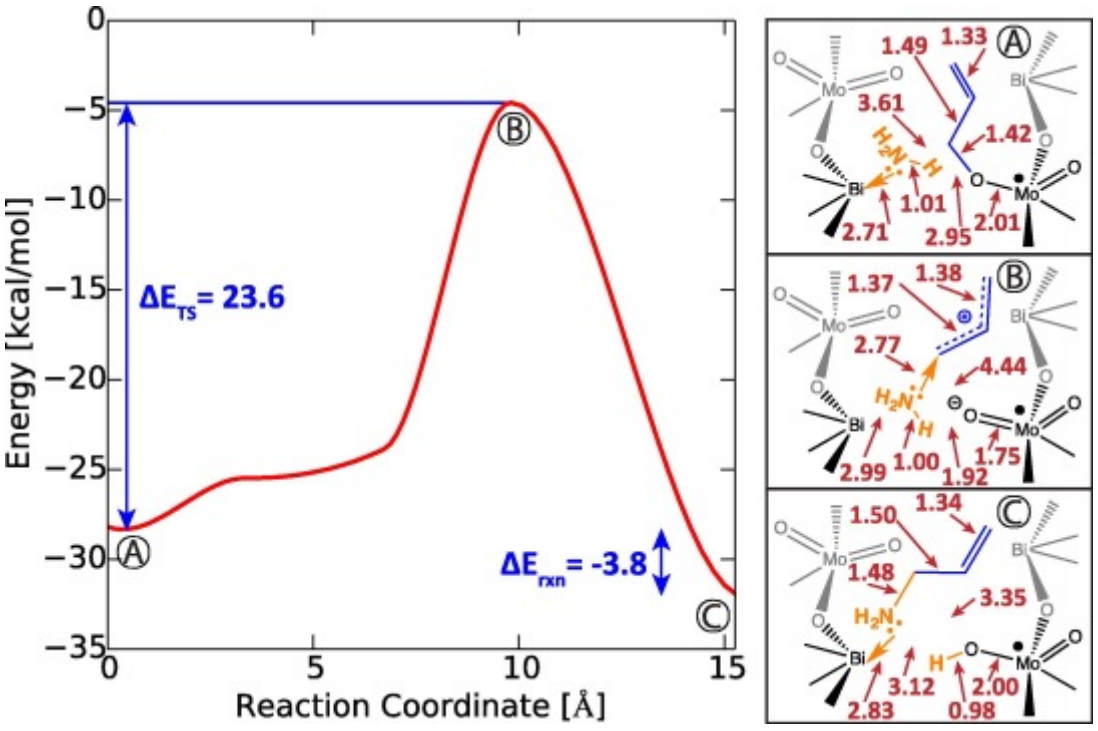

Download : Download high-res image (405KB) Download : Download full-size image

Fig. 7. Reaction barrier for reaction of allyl alkoxide and ammonia to produce adsorbed allylamine, with relevant energies annotated. Geometries for the initial state (A), t

(B) and final state (C) are shown on the right, with relevant distances in Å indicated. Reproduced with permission from Ref. 56 (ACS Catal., 7 (2017) 161–176). Copyright (2017) American Chemical Society.

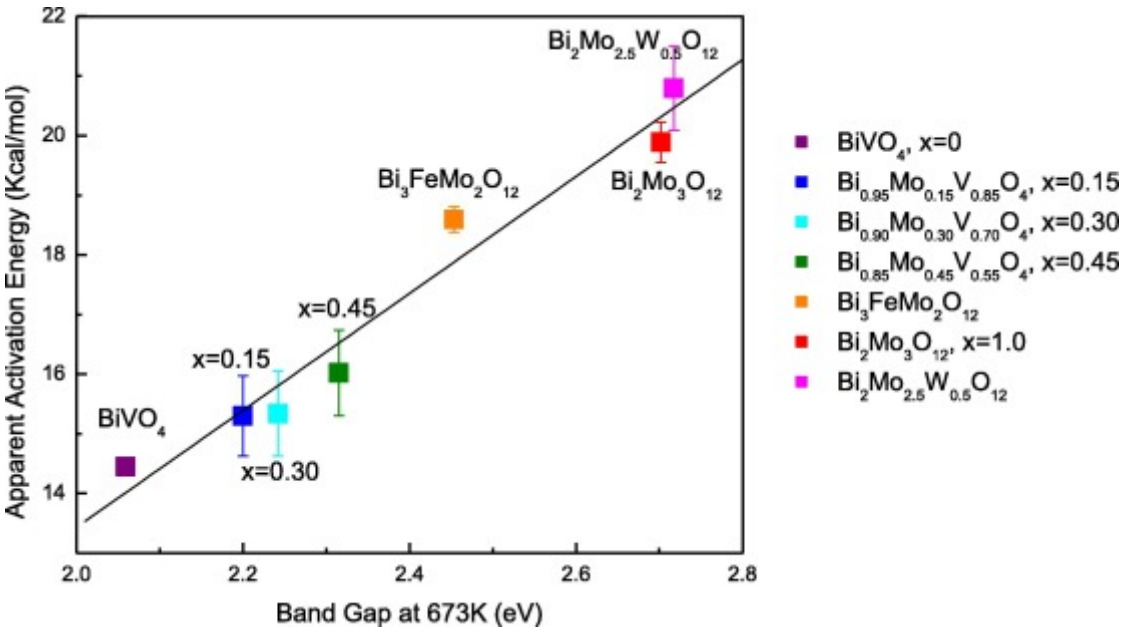

Download : Download high-res image (232KB) Download : Download full-size image

Fig. 8. Apparent activation energies for oxidation of propene to acrolein over substituted bismuth molybdates. Reproduced with permission from Ref. 62 Reproduced with permission from Ref. 56 (J. Am. Chem. Soc., 136 (2014) 13684–13697). Copyright (2014) American Chemical Society.

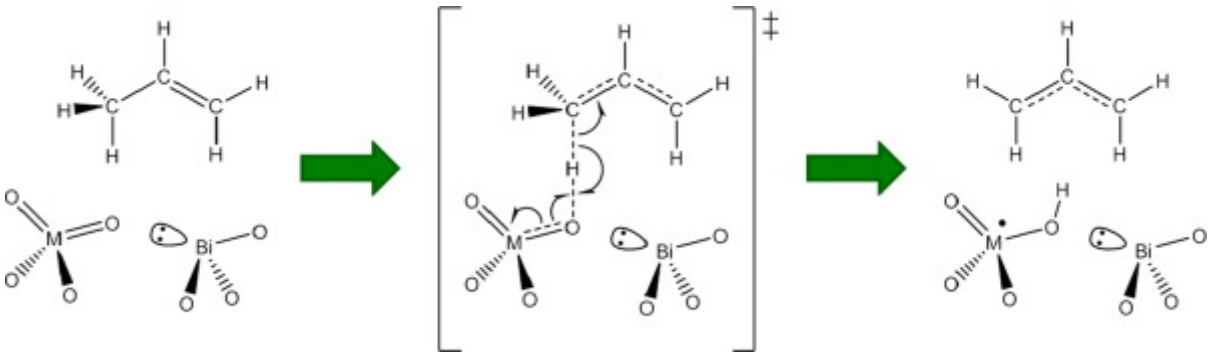

Download : Download high-res image (91KB) Download : Download full-size image

Fig. 9. Generic mechanism for propene activation involving a catalyst M=O bond. Reproduced with permission from Ref. 62 Reproduced with permission from Ref. 56 (J. Am. Chem. Soc., 136 (2014) 13684–13697). Copyright (2014) American Chemical Society.

The next step (**3 → 4**) is the addition of an allyl radical to a Mo═O group to create an energetically favored surface allyl alkoxide species. It is conceivable that this step occurs after the allyl radical diffuses from the site where it was generated to a nearby M═O group, since the activation energy for surface diffusion is ~2 kcal/mol is much lower than the barrier for step **2 → 1**, 7.5 kcal/mol. Experimental studies conducted with $^{18}O_2$ in the gas phase have shown that the O in the product acrolein comes from the catalyst surface, and not from gas phase oxygen [58]; therefore, the C—O bond formed in step **3 → 4** remains in the final product. Considering the bond distances given in Table 2, we see that the allyl species (**3)** shares one unpaired electron among the three carbon atoms, resulting in two ~1.5 order bonds, while in **4**, there is a clear terminal C_2-C_3 double bond and single bonds between Mo and O, O and C_1, and C_1 and C_2.

Step (**4 → 5**) is the second most energetically demanding step after the initial, rate-limiting step of propene activation, and involves abstraction of an H atom from the vinyl alkoxide species by a neighboring O═Mo^{6+}═O group to produce Mo-coordinated acrolein and a reduced neighboring site.

It is clear from Fig. 4 that abstraction of a hydrogen atom from the allyl alkoxide species to produce adsorbed acrolein is demanding, and the value of ΔE_{TS} for this step is only slightly lower than that for the initial hydrogen abstraction from propene. However, unlike the initial rate-limiting step of hydrogen abstraction, the final state for this step is significantly lower in energy than the transition state. This is because the radical species remaining after hydrogen abstraction is stabilized significantly by the bonding to oxygen and molybdenum that allows for more electron delocalization than is possible across only the three carbon atoms of the free allyl radical. Oxidation of the H abstraction site, **5,** produces structure **6**.

Structure **7** corresponds to adsorbed acrolein with a fully formed carbon-oxygen double bond and a reduced Mo^{4+}═O site. Acrolein adsorbs quite favorably at Bi^{3+} cations via donation of electron density from one of the lone pairs on oxygen to the under-coordinated bismuth cation. Note that **6 → 7** requires substantial rearrangement of the oxygen atoms around molybdenum, which is in a triplet state with an unpaired electron in each of two distinct d orbitals. The oxygen vacancy in **7** created upon acrolein formation is restored by atomic oxygen to form Structure **8**.

3.4. Mechanism of propene ammoxidation on the (0 1 0) surface of $Bi_2Mo_3O_{12}$

Scheme 1 shows the pathway for propene oxidation to acrolein in the presence of a spectator ammonia molecule (structure numbers are the same as in the case without ammonia but are now followed by an "N"). The energies for this pathway are shown in Fig. 6 so that they can be compared with those for the propene ammoxidation to acrylonitrile pathway shown in Scheme 2. In agreement with experiment the activation of propene to produce allyl radical (steps **0 → 3**, see Fig. 6) is common to all product pathways [10], [57].

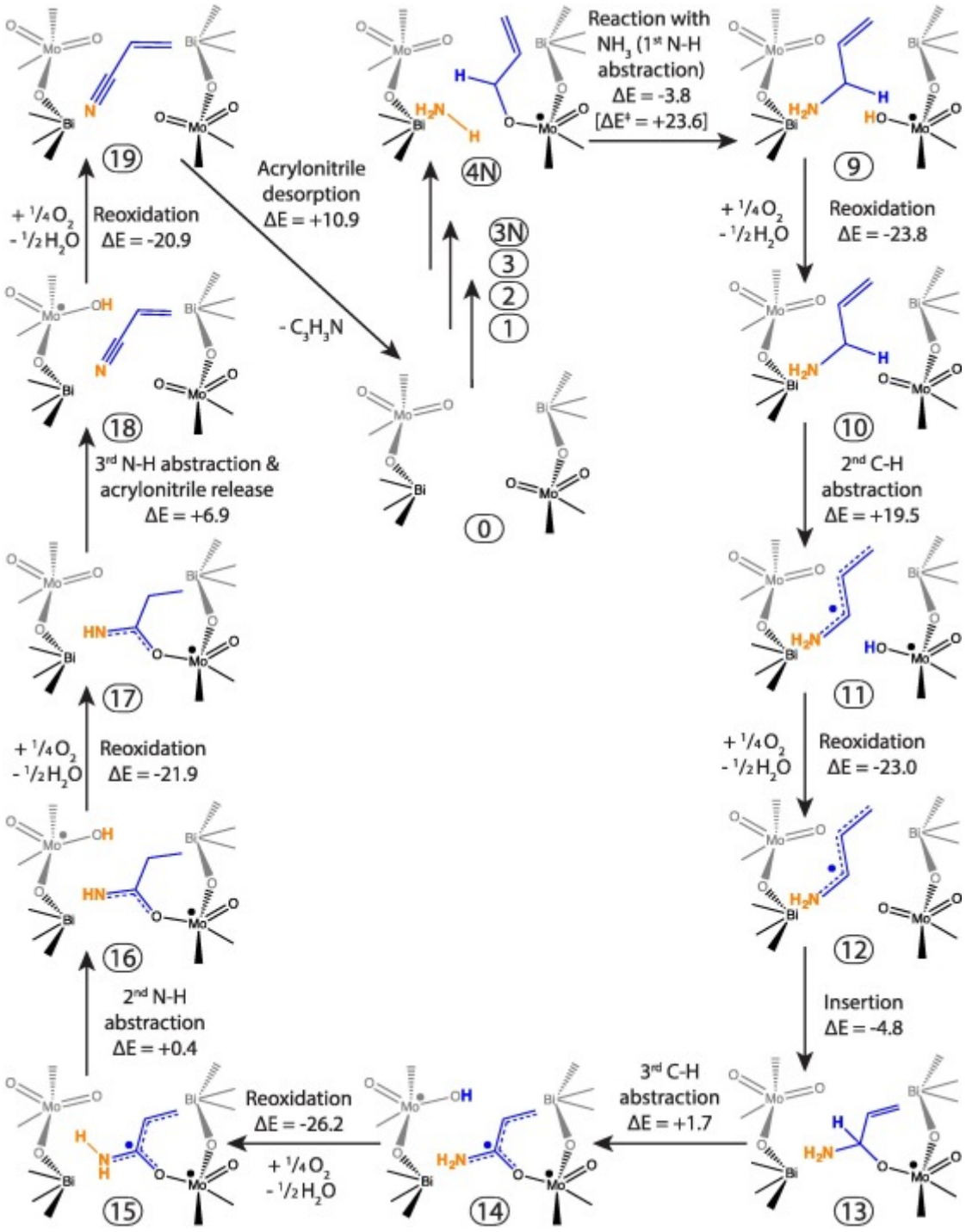

Download : Download high-res image (724KB) Download : Download full-size image

Scheme 2. Proposed elementary steps for propene ammoxidation to acrylonitrile (ΔE in kcal/mol). Reproduced with permission from Ref. 56 (ACS Catal., 7 (2017) 161–176). Copyright (2017) American Chemical Society.

C—N bonds are formed by reaction of allyl alkoxide species with adsorbed ammonia [59]. Ammonia adsorbs favorably on surface Bi^{3+} cations via sigma donation of electron

the lone pair on nitrogen to empty bismuth orbitals. The ammonia adsorption energy on Bi^{3+} is –17.9 kcal/mol on the fully oxidized surface. Since the acceptor orbitals of bismuth are very large and diffuse, ammonia can be anywhere in a ~2 Å x 2 Å area, as long as the nitrogen lone pair points toward a Bi^{3+} that is 2.6–3.0 Å away, and have approximately the same energy of adsorption. We find that adsorption of ammonia next to an adsorbed allyl (**3 → 3 N**) is essentially equivalent to ammonia adsorption on a bare catalyst surface (-17.2 vs. –17.9 kcal/mol).

The reaction of allyl alkoxide species with adsorbed ammonia in structure **4 N** produces allylamine, which then undergoes further reaction to form acrylonitrile (or acetonitrile and HCN). In Scheme 2, ammonia adsorbs on structure **3** to form **3 N**, which then undergoes allyl insertion to form **4 N**; however, ammonia could just as easily adsorb after insertion to form **4 N** directly from **4** or could already be present before the allyl radical is formed. While ammonia is shown to adsorb on the Bi^{3+} cation that perturbs the allyl alkoxide oxygen, ammonia could also adsorb on either of the two neighboring Bi^{3+} sites to either side of the allyl alkoxide species, since these sites are also close enough to allow reaction between the ammonia and the allyl alkoxide species.

The allyl alkoxide intermediate (**4 N**) can undergo one of two competing processes –abstraction of an H atom to form adsorbed acrolein and a neighboring Mo—OH group (**5 N**) or reaction with adsorbed ammonia to form adsorbed allylamine and a Mo—OH group (**9**). The activation barrier for step **4 → 5** is shown in Fig. 11. Comparison of the left- and right-hand sides of Scheme 1 shows that the presence of a spectator ammonia does not have a significant effect on the values of $\Delta E_{reaction}$. Since the adsorbed ammonia does not lie along the **4 → 5** reaction pathway, its presence should not affect the reaction barrier and therefore we assumed that ΔE_{TS} for **4 N → 5 N** is the same as for **4 → 5**.

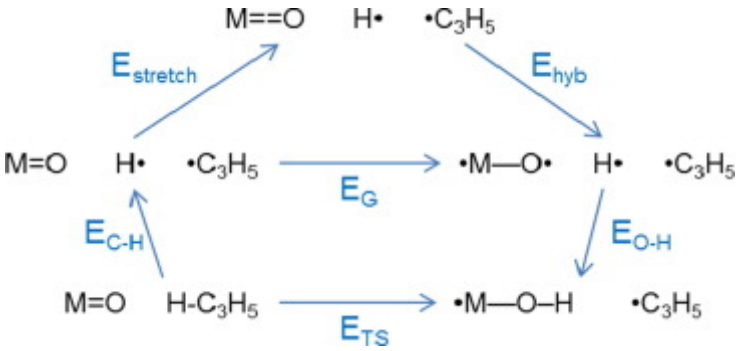

Download : Download high-res image (61KB) Download : Download full-size image

Fig. 10. Born-Haber cycle decomposition of the transition state energy E_{TS} into contributions from C—H bond breaking E_{C-H}, M=O bond elongation $E_{stretch}$, M=O bond rehybridization E_{hyb}, and O—H bond formation E_{O-H}. Reproduced with permission from Ref. 62 Reproduced with permission from Ref. 56 (J. Am. Chem. Soc., 136 (2014) 13684–13697). Copyright (2014) American Chemical Society.

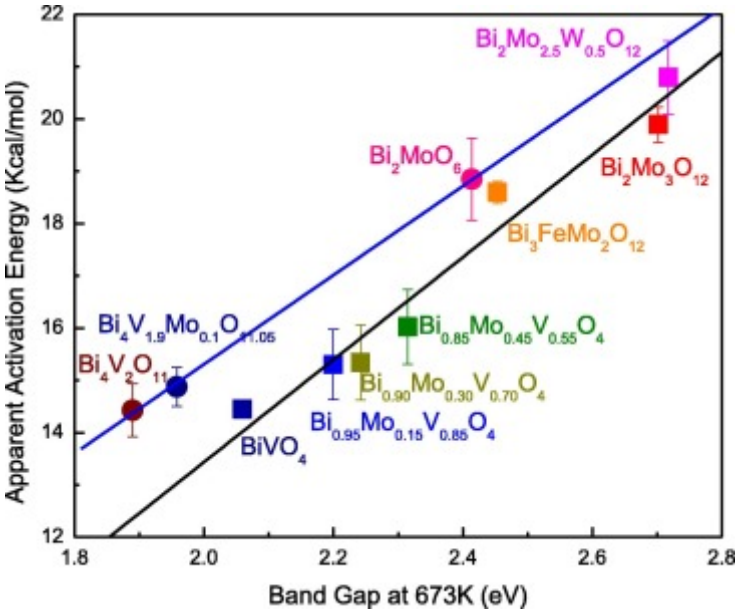

Download : Download high-res image (226KB) Download : Download full-size image

Fig. 11. Apparent activation energies for oxidation of propene to acrolein versus the band gap measured at 673 K for catalysts having the scheelite (lower line, square) and aurivillius (upper line, circle) structures. Reaction conditions: T = 673 K and $P_{C3H6} = P_{O2} = 0.167$ atm. Reproduced with permission from Ref. 66 (Catalysis Today 261 (2016) 146–153). Copyright (2014) Elsevier.

Our calculated potential energy for reaction of the allyl alkoxide species with ammonia to form allylamine is shown in Fig. 7. ΔE_{TS} is 23.6 kcal/mol and $\Delta E_{reaction}$ is –3.8 kcal/mol. Initial movement along the reaction pathway involves detachment of the allyl species, converting **4 N** back to **3 N**, so that the allyl species in **3 N** is favorably adsorbed above the bismuth cation. This part of the pathway accounts for the section of the reaction coordinate between 0 Å and 5 Å in Fig. 7. We found that the interaction between an allyl radical and a bismuth cation leads to a significantly lower reaction barrier than for the same pathway in which the allyl radical is further above the surface and thus not able to interact with the bismuth cation. The transition state for reaction **4 N → 9** involves an umbrella flip of ammonia, which removes the favorable lone pair interaction with the surface bismuth cation and forms a less favorable interaction with the electrophilic carbon of the allyl species. After the ammonia inverts, formation of the C—N bond followed by loss of a hydrogen atom to a surface molybdenyl oxo to form allylamine is highly exothermic. This reaction is a nucleophilic substitution reaction that most likely occurs by interaction of ammonia with an allyl cation to form allyl-NH_3^+ that then loses a proton to the oxygen anion to form allylamine. Once the allyl-NH_3^+ species loses a proton to the molybdenyl oxo, the nitrogen of allylamine can reform the favorable interaction with the surfa

cation that was lost in the transition state. The allylamine formed in reaction **4 N → 9** has the lowest adsorption energy of any species we investigated (ΔE_{ads} = –23.7 kcal/mol) because it has favorable, dative-type interactions from both the nitrogen lone pair and the carbon-carbon pi bond to two neighboring bismuth cations.

Overall, the activation barrier for allylamine formation is reasonably low because ammonia is stabilized by interaction with the carbon atom of the allyl species before it loses a hydrogen atom. The N—H bonds of ammonia (108.6 kcal/mol) are significantly stronger than the C—H bond of the methyl group of propene (88.2 kcal/mol) that is broken in the rate-limiting step. Alternative pathways for the interaction of ammonia with various hydrocarbon intermediate species were examined, but because of the high bond dissociation energy of the N—H bonds of NH_3, any reaction step that began with abstraction of an H atom from ammonia is not favorable. Therefore, ammonia can only be activated by $Bi_2Mo_3O_{12}$ once the nitrogen fragment formed upon hydrogen abstraction is first stabilized by favorable interaction with either the catalyst surface or a hydrocarbon species.

Comparing the reaction barrier of **4 N → 9** with **4 N → 5 N**, it is clear that production of allylamine is energetically favored by more than 10 kcal/mol over production of acrolein when a neighboring ammonia molecule is present. The transition state for allylamine formation is also likely to be entropically favored over the transition state for acrolein formation, since the former has two separate physisorbed molecules that have not yet come together, whereas the latter is highly constrained geometrically. Therefore, at reaction temperatures, if ammonia adsorbs at any of the three bismuth cations near an allyl alkoxide species, allylamine will always be produced. However, acrolein can still be formed via reaction **4 → 5** if ammonia is not adsorbed nearby. The ratio of acrylonitrile to acrolein is therefore only dependent on the ammonia adsorption, which is a function of ammonia partial pressure to the first order in this low coverage regime. Experimentally, the ratio of acrylonitrile to acrolein is approximately first order in ammonia partial pressure and the activation barrier for acrolein formation is ~15 kcal/mol higher than the barrier height for acrylonitrile formation at the same stage in the reaction sequence [60]. In summary, the DFT calculations for steps **4 N → 5 N** and **4 N → 9** are consistent with the difference in the activation energies determined from analysis of the reaction kinetics.

Once H atoms are abstracted from a reacting species onto the catalyst surface, the catalyst is reoxidized, e.g., steps **9 → 10**, **11 → 12**, **14 → 15**, **16 → 17**, and **18 → 19** (all indicated in Fig. 7 by hashed lines). These steps provide the thermodynamic driving force for all reactions involving the cleavage of C—H or N—H bonds.

Allylamine has two relatively weak C—H bonds, and should thus undergoes facile hydrogen abstraction. Since allylamine adsorbs quite strongly on the surface of $Bi_2Mo_3O_{12}$ via favorable electron donation from the nitrogen and from the carbon-carbon double bond to neighboring Bi^{3+} cations, it is unlikely to appear in the reaction products. Consistent with this projection, we observed a high conversion of allylamine when it was fed to the reactor under co

propene would only exhibit differential conversion [60]. The allyl–NH_2 radical species formed by abstracting one of these H atoms (Structure **11**) is significantly more stable than the allyl species formed in the rate-limiting step, since resonance structures involving both the lone pair on the nitrogen atom and the carbon-carbon pi bond electrons stabilize the radical. Therefore, the radical is delocalized across the entire fragment, resulting in all C—C and C—N bonds being 1.5 order.

Estimates of the activation barrier for reaction **10 → 11** suggest that this reaction has a singlet-triplet spin crossing transition state that is only a few kcal/mol higher in energy than the final state. A transition-state energy similar to the final-state energy is also observed for the initial hydrogen abstraction from propene (see above). Because of the high computational cost needed to determine singlet-triplet crossing transition states, this reaction barrier was not fully optimized. Since the difference between the transition state and the final state in the rate-limiting hydrogen abstraction from propene (step **1 → 2**) is only 7.6 kcal/mol, the very similar reaction of **10 → 11** is expected to have a transition state of ≤ 8 kcal/mol above the final state. Consequently, the activation of allylamine should be significantly less demanding (by approximately the 11.7 kcal/mol difference in their values of ΔE_{rxn}) than the activation of propene, and therefore will occur easily and not affect the overall rate of propene conversion.

We hypothesized initially that after formation of the allyl-NH_2 radical (**10 → 11**) and reoxidation of the catalyst surface (**11 → 12**), one of the H atoms from the NH_2 group would be abstracted to form 2-propen-1-imine (HN═CH-CH═CH_2), a compound similar to acrolein. However, all attempts to react this species resulted in very high positive values of $\Delta E_{reaction}$, due to the absence of any weak C—H or N—H bonds. Therefore, an alternate mechanism was considered, in which the allyl-NH_2 radical is first stabilized by addition to a surface molybdenum-oxygen double bond (**12 → 13**), thereby facilitating subsequent reactions. This reaction is the same as step **3 → 4** in the pathway for propene oxidation, except that the allyl species has a terminal —CH—NH_2 group instead of a terminal —CH_2 group.

The remaining alpha C—H bond of **13** is still quite labile and consequently its abstraction in step **13 → 14** is close to thermoneutral. The resulting tertiary carbon radical is highly stabilized by conjugation. The electron delocalization across the nitrogen, primary carbon and oxygen atoms results in a lengthening of the molybdenum-oxygen distance such that it is no longer a single bond.

After catalyst reoxidation (**14 → 15**), abstraction of one of the equivalent H atoms from the terminal NH_2 group occurs via another essentially thermoneutral process to form **16**. As noted above, N—H bonds are difficult to break. However, a hydrogen atom can easily be abstracted from **16**, because doing so regenerates the lone pair on nitrogen as the bond count on that atom goes from 3.5 to 2.5. This step is then followed by another oxidation step to form structure **17.** Consideration of the bond distances in analogous compounds that suggests that **16** and **17** have approximately 1.5 order bonds between the primary carbon and both nitrogen an

than the expected double bond to nitrogen and single bond to oxygen. These 1.5 order bonds to both nitrogen and oxygen are a result of both heteroatoms having lone pairs of electrons that can interact with the electrons on the primary carbon and the highly electrophilic oxygen pulling electron density from the —C═NH group.

The final N—H bond in **17** is reasonably strong and cannot be broken on its own. However, because this last hydrogen removal step can be coupled with breaking the carbon-oxygen bond to release the acrylonitrile, it still has a reasonable energy (**17 → 18**). Despite being mildly endothermic, this reaction will be favored entropically, since it releases a physisorbed product from a bound intermediate. Catalyst reoxidation (**18 → 19**) and desorption of acrylonitrile (**19 → 0**) completes the catalytic cycle. Since acrylonitrile does not have any weak C—H bonds, it is stable to further oxidation, which is what is observed when acrylonitrile is fed over the catalyst at standard reaction conditions [60].

3.5. Band gap as a descriptor of catalyst activity and selectivity for propene oxidation

The preceding discussion has shown that the ability of α-$Bi_2Mo_3O_{12}$ to activate propene is a consequence of the interaction of the lone pair of electrons on Bi^{3+} cations with proximate molybdenyl groups. This naturally leads to the question of whether other transition metal oxides having a scheelite structure similar to that of α-$Bi_2Mo_3O_{12}$ would be equally or less effective catalysts for promoting propene oxidation to acrolein. Since an oxygen atom at the catalysts surface must be sufficiently reactive to remove an H atom from the methyl group of propene, we explored the possibility that the band gap of the metal oxide catalyst might be a good descriptor of the reactivity of surface oxygen atoms. This choice was motivated by the recognition that hydrogen addition to surface oxygen involves bond formation using oxygen lone pair orbitals as well as electron transfer to unoccupied orbitals on adjacent transition metal centers. A descriptor that captures both the ability of oxygen to donate lone pair electron density and the ability of the transition metal to accept electron density is the ligand-to-metal charge transfer (LMCT) excitation energy. For metal oxides containing transition metal centers in their highest oxidation states, the LMCT excitation energy typically corresponds to the band gap energy. In chemical terms, the band-gap energy can be thought of as the energy difference between the highest occupied crystal orbital (which is typically oxygen-centered) and the lowest unoccupied crystal orbital (which is transition-metal centered). Since the band-gap energy contains information about the frontier molecular orbitals in a crystalline material, we explored whether the energy difference between frontier crystal orbitals in a mixed metal oxide can be used as a descriptor of catalytic activity.

Band structures were obtained for $Bi_{1-x/3}V_{1-x}Mo_xO_4$, $Bi_2Mo_3O_{12}$, and $Bi_3FeMo_2O_{12}$ by calculating the site projected density of states [60]. By default, the zero of energy in a VASP-generated density of states calculation is the energy of the highest occupied state. For this work we chose the reference zero energy to be the energy of the vacuum state (i.e., the energy of electrons and nuclei separated at infinity). Fig. 8 shows the apparent activation energy for each catalyst

function of the band gap energy measured at 673 K. This relationship can be understood by relating the band gap to the elementary processes involved in attaining the transition state for the rate-limiting step of propene oxidation, the step which involves cleavage of a C—H bond in the methyl group of the reactant.

To rationalize the correlation seen in Fig. 8, it is useful to consider a generic picture of the transition state for C—H activation over a surface M═O group (M = Mo, V). As shown in Fig. 9, the transition state for C—H bond activation involves three simultaneous processes: dissociation of a C—H bond, formation of an O—H bond, and elongation and rehybridization of an M═O double bond to yield an M—O single bond. The sum of these three processes can be written as $M^{(n)+} = O^{2-} + C_3H_6 \rightarrow {}^{\bullet}M^{(n-1)+}–OH + {}^{\bullet}C_3H_5$.

Fig. 10 illustrates how the contributions from each of the three components to the overall reaction barrier can be represented in terms of a Born Haber cycle. The bond dissociation energy for a C—H bond in the methyl group of propene is 88.2 kcal/mol [61]. The remaining contributions are summarized in Table 3. The H bond formation energy E_{OH} was determined by calculating the energy released by the attachment of an H radical to ${}^{\bullet}M—O{}^{\bullet}$. A value of ΔE_{OH} of 117.9 kcal/mol was obtained for M═Mo, and 115.8 kcal/mol for M═V, suggesting that the O—H bond energy does not depend strongly on the identity of the nearest neighbor to oxygen. For comparison, the dissociation energy for the first O—H bond in water is 117.59 kcal/mol [62].

Table 3. Measured and calculated band-gap energies (E_G) and calculated values for E_{strech}, E_{hyb}, and E_{OH}. Reproduced with permission from Ref. 62 Reproduced with permission from Ref. 56 (J. Am. Chem. Soc., 136 (2014) 13684–13697). Copyright (2014) American Chemical Society.

	$BiVO_4$	$Bi_2Mo_3O_{12}$
E_G from DRUVS at 673 K	2.06 eV	2.70 eV
E_G from DFT	2.28 eV	2.80 eV
$E_{stretch}$	20.9 kcal/mol	23.0 kcal/mol
E_{hyb}	30.1 kcal/mol	39.0 kcal/mol
E_{OH}	–115.8 kcal/mol	–117.9 kcal/mol

The value of $E_{stretch}$ was determined by subtracting the energy of the model catalyst surface with the active site M═O bond at the M—O bond distance of the initial state for C—H bond activation (1.60 Å for V═O, 1.74 Å for Mo═O) from the energy of the model catalyst surface with the active site M═O bond stretched to the M—O bond distance in the M—OH f

for V-O, 2.00 Å for Mo—O). Again, the values of $E_{stretch}$ are similar for $BiVO_4$ and $Bi_2Mo_3O_{12}$. Remarkably, the 2.1 kcal/mol greater $E_{stretch}$ required to elongate the Mo═O bond is exactly matched by a 2.1 kcal/mol greater Mo—OH bond strength. This cancelation may indicate a compensation effect whereby the M—O bond undergoes a greater (more energetically costly) deformation in order to form a stronger M—OH bond.

E_{hyb} was calculated as the difference in energy between singlet M═O and triplet •M—O• orbital configurations for the M—O bond at the final state (M—OH) geometry (but with no H atom attached), and reflects only the energy required to rearrange electron density within the M—O bond [63]. As seen in Table 3, the largest difference between $BiVO_4$ and $Bi_2Mo_3O_{12}$ occurs for the E_{hyb} term. Furthermore, the compensation between $E_{stretch}$ and E_{OH} eliminates the composition dependence of the sum $E_{stretch} + E_{OH}$; as a result, almost the entire difference in E_{TS} between $BiVO_4$ and $Bi_2Mo_3O_{12}$ is due to the E_{hyb} term. Importantly, the metal-oxygen bond reorganization energy described by E_{hyb} — transfer of an electron from a non-bonding oxygen 2p-derived state into a metal d-derived state with π*(M═O) antibonding character — corresponds to an LMCT excitation. Both the M—O bond reorganization taking place at the C—H bond activation transition state and the LMCT excitation that gives rise to the band gap involve the M═O → •M—O• redistribution of electron density. It is for this reason that the band gap energy emerges as a descriptor of catalytic activity.

Correlation of the activation energy with the band-gap observed for metal oxide catalysts with the scheelite structure also hold for metal oxides having the aurivillius structure [64]. Fig. 11 shows that the apparent activation energy for propene oxidation correlates linearly with the band gap for catalyst of different composition having either the scheelite or aurivillius structure. The only difference is that for the same band gap, the apparent activation energies are about 1.5 kcal/mol higher for catalysts with the aurivillius than the scheelite structure. Since the apparent activation energy is the sum of the enthalpy of propene adsorption and the intrinsic activation energy, we propose that the slightly higher activation energies observed for catalysts with the aurivillius structure compared to the scheelite structure is due the slightly more favorable heat of adsorption for propene on the former structure.

The results presented in Fig. 11 indicate that catalysts with low band gaps should be exhibit a higher activity for propene oxidation to acrolein per active site than those with higher band gaps. As illustrated in Fig. 12, while this conclusion is true for catalysts with band gaps above about ~2.1 eV, it does not hold for catalyst with lower band gaps. Once the band gap falls below 2.1 eV, the surface oxygen atoms become sufficiently active that they can attack the precursor to acrolein and divert it to CO and CO_2 [65]. Thus, $Bi_{0.95}Mo_{0.15}V_{0.85}O_4$, which has a band gap of 2.2 eV, exhibits the lowest activation energy for propene oxidation (~15 kcal/mol) while maintaining a high selectivity (82%).

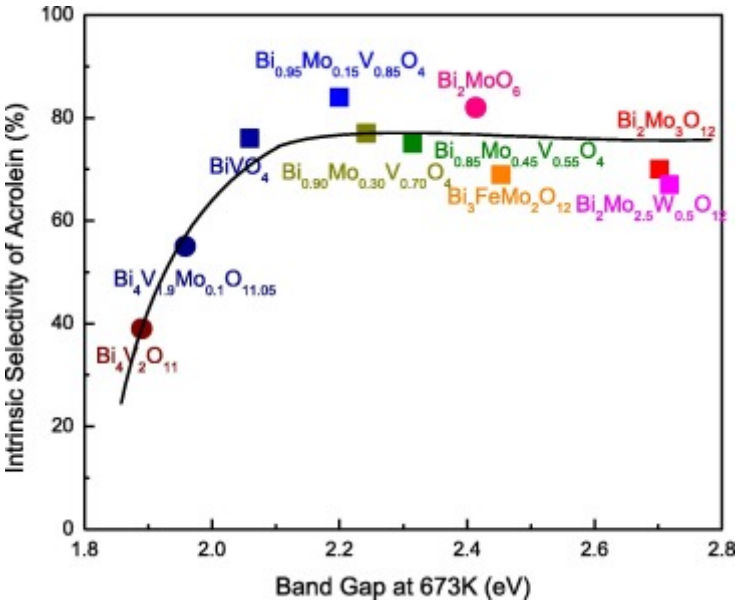

Download : Download high-res image (170KB) Download : Download full-size image

Fig. 12. Intrinsic selectivity to acrolein versus the band gap measure at 673 K (scheelite, square; aurivillius, circle). Reaction conditions: T = 673 K and $P_{C3H6} = P_{O2} = 0.167$ atm. Reproduced with permission from Ref. 66 (Catalysis Today 261 (2016) 146–153). Copyright (2014) Elsevier.

The effects of lattice structure on the activity and selectivity of bismuth molybdates for propene oxidation have also been examined by Grunwaldt and coworkers [65]. For this study, the authors prepared samples of α-$Bi_2Mo_3O_{12}$ and β-$Bi_2Mo_2O_9$, both of which have the scheelite structure, and a sample of γ-Bi_2MoO_6, which has an aurivillius structure. The structure of these materials was confirmed by X-ray diffraction and Raman spectroscopy. Fig. 13 shows the acrolein (a) and CO/CO_2 (b) selectivities for each catalyst as a function of the measured propene conversion at 678 K. This figure shows that the acrolein selectivity is higher and the CO/CO_2 selectivity is lower for the catalysts having a scheelite structure, and that the sensitivity of these selectivities to increasing propene conversion is greater for the catalyst with the aurivillius structure. It is notable, though, one catalyst, FSP-c, which begins as γ-Bi_2MoO_6 but evolves to a mixture of γ-Bi_2MoO_6, α-$Bi_2Mo_3O_{12}$, and β-$Bi_2Mo_2O_9$, exhibits the highest selectivity to acrolein and the least loss of the selectivity with increasing propene conversion. The authors hypothesize that the high acrolein selectivity of this catalyst may be its avoidance of forming a Bi_2O_3 phase, which exhibits a high activity for reacting the nascent allyl radicals with molecular O_2 and thereby diverts these radicals to form CO/CO_2 instead of acrolein.

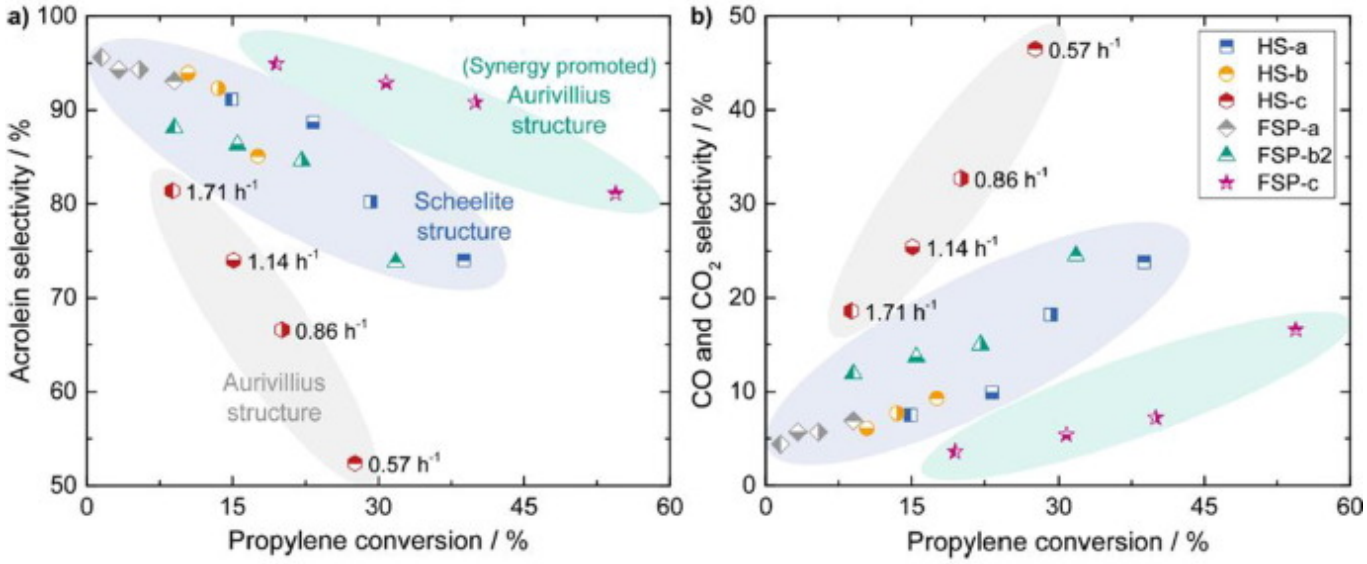

Download : Download high-res image (256KB) Download : Download full-size image

Fig. 13. Acrolein selectivity (a) and CO/CO_2 selectivity (b) vs propene conversion for bismuth molybdates. Reaction conditions: T = 678 K, feed composition $N_2/O_2/H_2O/C_3H_6$ = 70/14/8/8, and WHSV = 0.57–1.71 h^{-1}. Catalysts: HS-a and FSP-a are α-$Bi_2Mo_3O_{12}$; HS-b and FSP-b are β-$Bi_2Mo_2O_9$, HS-c γ-Bi_2MoO_6, and FSP-c is a mixture of γ-Bi_2MoO_6, α-$Bi_2Mo_3O_{12}$, and β-$Bi_2Mo_2O_9$. HS stand for hydrothermal synthesis and FSP stands for flame spray synthesis. Reproduced with permission from Ref. 67 (ACS Catal., 8 (2018) 6462–6475). Copyright (2018) American Chemical Society.

A detailed examination of the mechanism and kinetics of forming unselective products during the oxidation of propene to acrolein over α-$Bi_2Mo_3O_{12}$ has been reported by Bui et al. [66]. The principal products observed were acrolein, acetaldehyde, acetone, acrylic acid, acetic acid, ethylene, butadiene, benzene, CO, and CO_2. The yields of these products as a function of propene conversion are presented in Fig. 14, and Table 4 lists the carbon selectivities for each product for a propene of 0% and 25%. By feeding observed products together with propene the authors were able to assess whether a given compound is a primary product and is unstable and undergoes further oxidation (i.e., acrolein, acetaldehyde, acetone, and acetic acid), or, alternatively, is a secondary product (i.e., ethylene, butadiene, and benzene). It is notable that CO and CO_2, the most significant byproducts are both primary and secondary products. The mechanism shown in Scheme 3 was used to represent the kinetics for forming each of the products listed in Table 4 and the rate parameter for each step were obtained by fitting the predicted yield of product to experimental data taken over a wide range of conditions. The authors also discuss how lattice oxygen, surface hydroxyl group, and adsorbed O_2 may participate in each of the steps shown in Scheme 3.

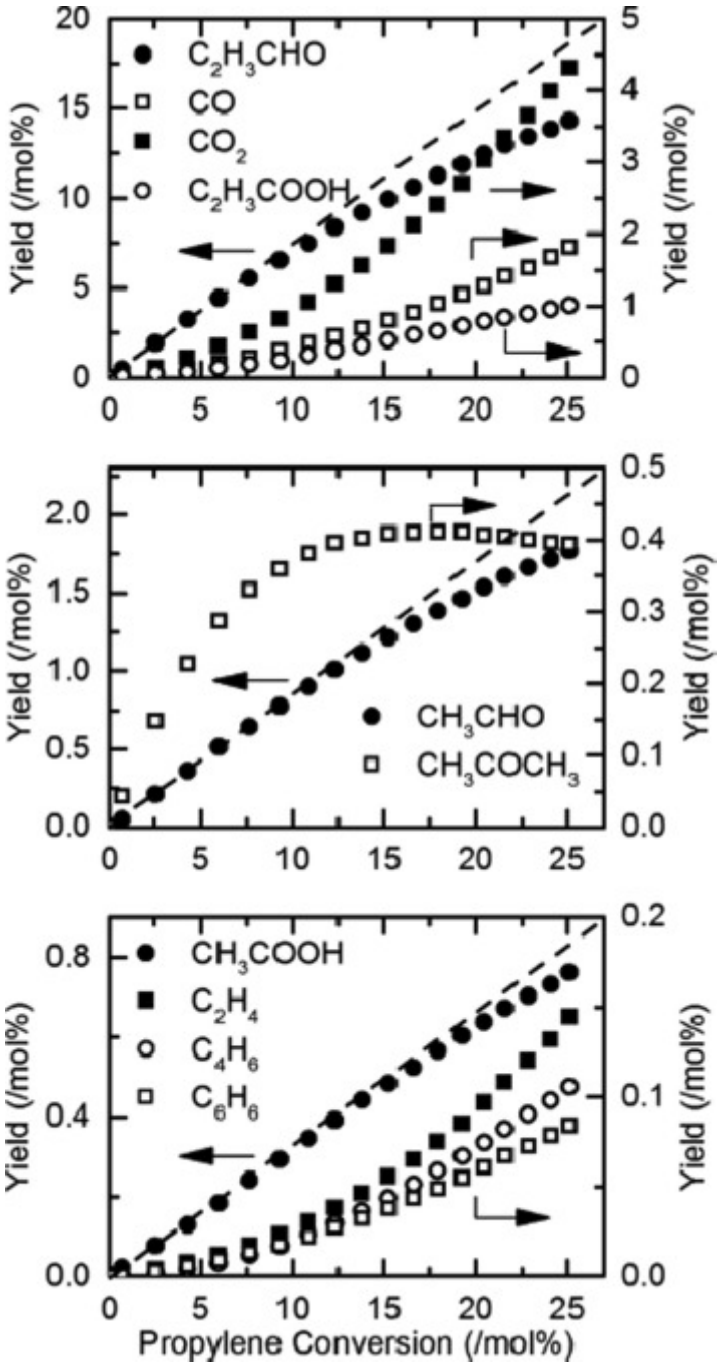

Download : Download high-res image (330KB) Download : Download full-size image

Fig. 14. Yields (on a carbon basis) of the propylene oxidation products on α-$Bi_2Mo_3O_{12}$ with respect to propylene conversion as assessed in a gradient-less recirculating batch reactor. Reaction parameters: 400 mg of $Bi_2Mo_3O_{12}$, 623 K, initial reaction mixture comprised of 6 kPa propylene, 7 kPa oxygen, and 7 kPa water. Reproduced with permission from Ref. 68 (ACS Catal., 6 (2016) 6567–6580). Copyright (2016) American Chemical Society.

Table 4. Product orders and stabilities for propene oxidation over $Bi_2Mo_3O_{12}$ at 623 K up to 25% conversion. Reproduced from with permission from Ref. 68 (ACS Catal., 6 (2016) 6567–6580). Copyright (2016) American Chemical Society.

		Carbon selectivity (%)	
Product	**Product order and stability**	**Initial[a]**	**At 25% Conversion**
Acrolein	**Primary unstable**	74	57
CO	**Primary and secondary**	2.0	7.2
CO_2	**Primary and secondary**	4.0	17
Acrylic acid	**Secondary**	1.4	4.0
Acetaldehyde	**Primary unstable**	8.6	7.0
Acetone	**Primary unstable**	6.9	1.6
Acetic acid	**Primary unstable**	3.0	3.0
Ethylene	**Secondary**	0.11	0.57
Butadiene	**Secondary**	0.07	0.42
Benzene	**Secondary**	0.08	0.34
Others		0	<0.1

a Extrapolated values to zero prolyene conversion.

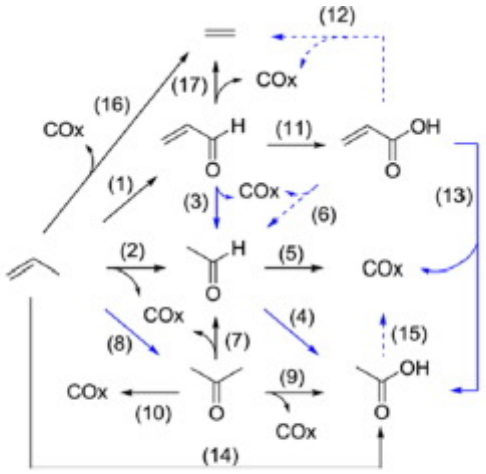

[a]The black arrows represent reactions whose rates are independent of water pressure. The solid blue arrows represent reactions that are promoted by water, while the dashed blue arrows represent reactions that are inhibited by water.

Download : Download high-res image (162KB) Download : Download full-size image

Scheme 3. Proposed scheme for propene oxidation on a-$Bi_2Mo_3O_{12}$ at 623 K. Reproduced with permission from Ref. 68 (ACS Catal., 6 (2016) 6567–6580). Copyright (2016) American Chemical Society.

3.6. The role of Bi^{3+} cations in forming active sites in molybdate catalysts

It is notable that all of the catalysts exhibiting high activity for propene oxidation and ammoxidation contain Bi^{3+} cations. As discussed above, Bi^{3+} cations electronically perturb the neighboring surface molybdenyl oxo groups in $Bi_2Mo_3O_{12}$ and, in doing so, enhance the activity of these sites for propene activation via abstraction of a hydrogen atom from the methyl group of adsorbed propene [56]. This influence of Bi^{3+} cations is attributed to electronic repulsion between the bismuth lone pair and an oxygen 2p lone pair, which destabilizes the Mo═O singlet state, and from back donation from the ▪Mo–O▪ π* orbital to the bismuth 6p orbital, which stabilizes the triplet state. The combination of these electronic effects leads to a lower singlet → triplet excitation energy, and thus lowers the transition-state barrier for hydrogen abstraction from propene. However, the magnitude of this effect is estimated to be only ~3 kcal/mol, which is insufficient to explain the overall difference in activity between $Bi_2Mo_3O_{12}$ and other molybdenum-oxide-based materials. To gain deeper insights into the effects of composition and local structure of the active site, we investigated oxides containing molybdenum as the only redox-active metal, thereby allowing us to focus on the effects of crystal structure, Mo coordination, and the identity of additional elements [67]. The four metal oxides investigated were MoO_3, $Bi_2Mo_3O_{12}$, $PbMoO_4$, and $Bi_2Pb_5Mo_8O_{32}$.

To be active a catalyst propene oxidation and ammoxidation, a catalyst must have an active oxygen atom for hydrogen abstraction and a favorable propene adsorption site near the active oxygen atom. To probe these features the energies shown in Fig. 15 were calculated for $Bi_2Mo_3O_{12}$, $PbMoO_4$, $Bi_2Pb_5Mo_8O_{32}$ and MoO_3. For each material, zero relative energy corresponds to the bare oxidized surface plus propene in the gas phase. $\Delta E_{ads,C3H6}$ is the energy change upon propene adsorption on the oxidized surface and is always negative. ΔE_{rxn} is the overall energy of reaction to go from adsorbed propene to adsorbed allyl radical and a hydrogen atom added to a Mo═O group. This hydrogen abstraction process has an activation barrier, shown in grey in Fig. 15. The transition-state energy is designated as ΔE_{TS}. At the high temperature required for propene oxidation and ammoxidation (~600–700 K), entropy dominates adsorption, and the catalyst resting state is the bare oxidized surface plus gas-phase propene. Therefore, as indicated by $E_{a,app}$ in Fig. 15, the apparent activation energy for hydrogen abstraction from propene will be the energy difference between the transition state and the bare oxidized surface with propene in the gas phase.

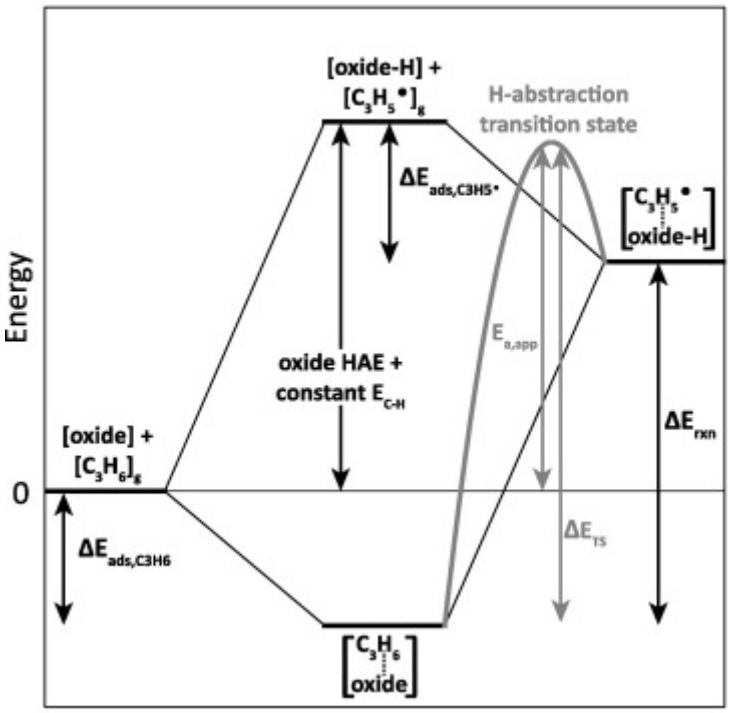

Download : Download high-res image (168KB) Download : Download full-size image

Fig. 15. Diagram depicting calculated energy values. Reproduced with permission from Ref. 69 (J. Phys. Chem. C, 120 (2016) 629233–29247). Copyright (2016) American Chemical Society.

We calculated the activation barrier for hydrogen abstraction from propene adsorbed on $Bi_2Mo_3O_{12}$ to be ΔE_{TS} = 38.8 kcal/mol [55]. As noted earlier (see Fig. 5) this reaction occurs via a singlet-triplet spin-crossing transition state that is only 7.6 kcal/mol above the fi

final state, the allyl radical is weakly adsorbed on the oxide surface and has a geometry and energy that are quite similar to those of the transition state. Since determination of the transition state is computationally intensive, due to the slow convergence of calculations done with the M06-L functional, we compared the properties of different oxides on the basis of the structure and energy of the final state attained after hydrogen abstraction from propene and used this energy as a measure of the relative apparent activation energies for hydrogen abstraction from propene on different oxides. We note that the energy of the final state is clearly a lower bound on the apparent activation energy, since the transition state must be higher in energy than the energy of the final state.

Another metric we use is the Hydrogen Attachment Energy (HAE), which is a measure of the hydrogen abstraction ability of various surface oxygen atoms. The HAE is defined as the energy difference between an all-electron-paired bare catalyst surface plus a gas phase hydrogen atom (with a single electron) and the catalyst surface with the hydrogen atom attached to a surface oxygen and thus one unpaired electron, as in Eqn. (1).

$$HAE = E_{H\text{-}surf} - (E_{surf} + E_H) \quad (1)$$

Fig. 18 demonstrates that the energy of the final state is the sum of HAE, the bond dissociation energy of a hydrogen on the methyl group of propene $E_{C\text{-}H}$, and the adsorption energy for the allyl radical $\Delta E_{ads,C3H5\cdot}$. Since $E_{C\text{-}H}$ it is independent of the catalyst and $\Delta E_{ads,C3H5\cdot}$ is expected to be similar in magnitude to the propene adsorption energy $\Delta E_{ads,C3H6}$, we use the value HAE to determine the most active surface oxygen atom on each material.

As noted in Table 5, there are four types of oxygen atoms on the surface of the oxides studied. The first, O_α, is a pure molybdenum-oxygen double bond with a bond length less than or equal to 1.70 Å. The second type, O_β, is an oxygen atom doubly bonded to Mo that is electronically perturbed by a neighboring atom (X), resulting in a slightly longer Mo—O distance, between 1.70 and 1.76 Å. The third type, O_γ, has two single bonds to two different atoms (Mo and X), resulting in a molybdenum-oxygen distance of 1.76–2.00 Å. Finally, the fourth type, O_δ, has two single bonds to two atoms and is also loosely coordinated to a nearby molybdenum atom at a distance of 2.00–2.40 Å. Beyond a Mo—O distance of 2.40 Å, there is no specific interaction between the two atoms.

Table 5. Types of surface oxygen atoms, where X can be either Mo or another atom. Reproduced with permission from Ref. 69 (J. Phys. Chem. C, 120 (2016) 629233–29247). Copyright (2016) American Chemical Society.

Oxygen Name	Mo—O distance (d) range [Å]	Depiction	Description

Oxygen Name	Mo—O distance (d) range [Å]	Depiction	Description
O_α	≤ 1.70	Mo═O	Pure double bond
O_β	1.70 < d < 1.76	Mo═O----X	Electronic perturbation by X
O_γ	1.76 ≤ d < 2.00	Mo—O—X	Two single bonds
O_δ	2.00 ≤ d < 2.4680	Mo----O	Loose coordination

Table 6 lists the HAE and the surface geometry before and after hydrogen addition for each of the four metal oxide materials. These data can be used to identify what geometries lead to a low HAE. As will be shown, increased coordination of molybdenum 6 + cations by oxygen anions significantly lowers the value of the HAE. We also find that the ability of the surface to distort upon hydrogen addition and therefore coordinate molybdenum with an additional bulk oxygen atom positioned *trans* to the oxygen atom to which the hydrogen was added is critical for achieving a favorable HAE Table 7.

Table 6. Hydrogen addition energy (HAE) for each of the surface oxygen atoms in the mixed metal oxides examined (the O atom used in Figure 18 is indicated by bold font). Reproduced with permission from Ref. 69 (J. Phys. Chem. C, 120 (2016) 629233–29247). Copyright (2016) American Chemical Society.

Material	Type of Surface Oxygen	HAE (kcal/mol) Full surface relaxation *[hydroxyl relaxation only]*
$Bi_2Mo_3O_{12}$	O_α	–52.9 *[–45.8]*
	O_β	**–58.3 *[–47.2]***
	O_γ	–45.5
$PbMoO_4$	O_β	–44.0
$Bi_2Pb_5Mo_8O_{32}$	O_β	–44.7
	O_β'	**–47.6 *[–40.3]***
	O_β''	–43.4
	O_γ	–43.9
MoO_3	**O_α**	**–58.2 *[–54.8]***
	O_β	–63.2 *[–36.1]*

Table 7. Propene adsorption energy on an oxidized surface ($\Delta E_{ads,C3H6}$) and allyl adsorption energy on a one hydrogen added surface ($\Delta E_{ads,C3H5}$) for each of the four tested materials. Reproduced with permission from Ref. 69 (J. Phys. Chem. C, 120 (2016) 629233–29247). Copyright (2016) American Chemical Society.

Material & Surface Oxygen	$\Delta E_{ads,C3H6}$ on oxidized surface [kcal/mol]	$\Delta E_{ads,C3H5}$ on 1-H surface [kcal/mol]
$Bi_2Mo_3O_{12}$ [O_β]	–11.5	–12.0
$PbMoO_4$ [O_β]	–8.2	–9.0
$Bi_2Pb_5Mo_8O_{32}$ [O_β']	–10.3	–10.4
MoO_3 [O_α]	–1.8	–6.4

Fig. 16 displays the relevant energy parameters for the most active surface oxygen on the four metal oxide surfaces studied. The energy of the final state, allyl radical adsorbed over a surface with one hydrogen atom added to a Mo═O group, relative to the zero-energy reference state of bare oxidized surface with propene in the gas phase is a measure of the ability of the catalyst to activate propene. As discussed above, the energy of this final state is a lower bound on the apparent activation energy. For $Bi_2Mo_3O_{12}$, the only material for which we have calculated the full reaction barrier, the transition state is only 7.6 kcal/mol above the final state [42], [55]. Given what we know from the Born-Haber cycle decomposition of the transition state energy [61], we expect that the combination of HAE and propene adsorption captures the major components of the transition state, and therefore we expect that the other materials have actual transition state energies that are similarly close in energy to the final state. However, regardless of the difference between the two, the transition state cannot be lower in energy than the final state.

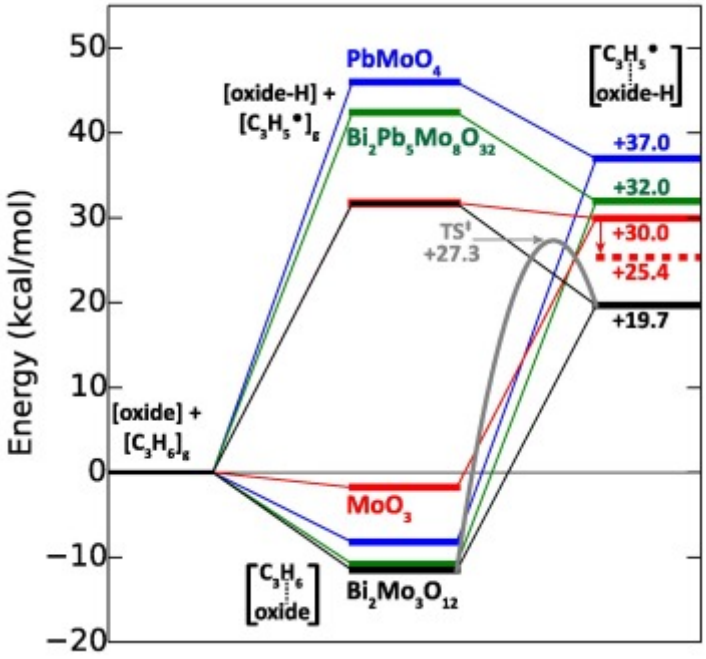

Download : Download high-res image (243KB) Download : Download full-size image

Fig. 16. Relevant energy values for first hydrogen abstraction from propene. Normalization point for all materials is a bare oxidized surface plus propene in the gas phase. Full reaction barrier through the transition state shown only for $Bi_2Mo_3O_{12}$. The two final state values for MoO_3 are shown, one for $\Delta E_{ads,C3H5} = \Delta E_{ads,C3H6}$ (solid line) and one for calculated $\Delta E_{ads,C3H5}$ (dashed line). The appropriate comparison between materials is the energy of the final state indicated with a solid line. Reproduced with permission from Ref. 69 (J. Phys. Chem. C, 120 (2016) 629233–29247). Copyright (2016) American Chemical Society.

Fig. 16 demonstrates that $Bi_2Mo_3O_{12}$ is a good catalyst for propene activation because it has a low energy for propene adsorption near the most active oxygen, which itself has a low HAE. Taken together, these effects combine to give a final state energy of 19.7 kcal/mol, the lowest of any material examined in this study. Moreover, the character of the Bi orbitals allows for favorable dative interaction between propene and bismuth to be partially maintained in the transition state, which should help stabilize the allyl radical as it forms [55].

4. Conclusions

The oxidation and ammoxidation of propene to acrolein and acrylonitrile are important industrial processes. While the catalyst for both processes have undergone considerable evolution during the past 60 years, all continue to be based on bismuth molybdates. The commercial importance of propene oxidation and ammoxidation has stimulated significant efforts to understand the mechanism and kinetics of these reactions. Given the central role

molybdates, the majority of these studies have focused α-$Bi_2Mo_3O_{12}$, since it exhibits both high activity and stability. This review highlights the wealth of information on the mechanism and kinetics of propene oxidation and ammoxidation on α-$Bi_2Mo_3O_{12}$ that have been obtained from experimental studies and then illustrates how theoretical studies provide support for the conclusions drawn from experimental efforts and, more importantly, provide a deeper understanding of the reaction mechanism and the unique role of bismuth in defining the effectiveness of bismuth molybdates.

Experimental studies have shown that the kinetics of both reactions are first order in propene partial pressure and zero order in oxygen partial pressure, and in the case of propene ammoxidation, zero order in ammonia partial pressure. These observations, together with D labeling experiments, suggest that both reactions are rate-limited by activation of a C—H bond in the methyl group of propene to form a symmetrical allyl radical. The occurrence of this intermediate is supported by experiments conducted with ^{13}C labeled propene. The zero order in oxygen partial pressure suggests that under reaction condition, the surface of the catalyst is saturated with oxygen and that the oxygen atoms involved in the activation of the methyl group C—H bonds of propene derive from the catalyst, and not adsorbed O_2. This conclusion is supported by ^{18}O labeling experiments. The question of which elements undergo reduction/oxidation during propene oxidation has been addressed using X-ray absorption spectroscopy, which shows that Mo^{6+} cations reduce to Mo^{4+} cations but Bi^{3+} cations are not reduced. It is also found that under steady-state propene oxidation, Mo remains in its fully oxidized state, indicating the rate of Mo^{4+} oxidation to Mo^{6+} is much more rapid that the rate of Mo^{6+} reduction.

Theoretical studies provide additional information about the mechanism of propene oxidation and ammoxidation. Our work has shown that physically meaningful DFT calculations require a realistic model of the surface of a-$Bi_2Mo_3O_{12}$ and combined with a density functional and basis set that are able to correctly reproduce the geometry and band gap of the oxide, as well the electronic states of adsorbed intermediates. Using this approach, we have found that the most energetically demanding reaction is C—H bond activation of a methyl group in propene. This step occurs preferentially at bismuth-perturbed Mo═O groups via a singlet-to-triplet spin-state crossing, which is highly probable due to favorable spin-orbit coupling. This reaction has an intrinsic activation barrier of 38.8 kcal/mol. Favorable propene adsorption, a consequence of electron donation from the carbon-carbon pi bond to under-coordinated surface Bi^{3+} cations, results in an apparent activation energy of 27.3 kcal/mol in reasonable agreement with experimental observation. The transition state for hydrogen abstraction is similar in both energy and geometry to the product state, which is a high-energy π-allyl radical. Rapid and energetically favorable catalyst reoxidation drives the activation reaction forward, offsetting the occurrence of the reverse reaction. The π-allyl radical formed by propene activation is stabilized by reaction with a Mo═O group to form an allyl alkoxide. This species can then either undergo abstraction of its alpha hydrogen to form a surface-coordinated acrolein or reaction with NH

dative bond on a proximate Bi^{3+} cation, to form allylamine. We show that the activation barrier for the latter process is significantly lower than for the former, consistent with the experimental observations that, in the presence of gas-phase ammonia, acrylonitrile is formed preferentially to acrolein, and that the selectivity to acrolein increases with increasing temperature. In agreement with our experimental results, our calculations confirm that allylamine is a viable intermediate on the pathway to acrylonitrile. Reaction of allylamine occurs by sequential abstraction of the four hydrogen atoms in order of increasing bond dissociation energy, with stabilization of the intermediate species via bonding with a surface molybdenyl oxo species.

Our theoretical approach also explains the positive correlation of the apparent activation energy for propene oxidation to acrolein with the band gap for bismuth molybdate containing vanadium, tungsten, or iron in either scheelite or aurivillius phases. A Born-Haber analysis of the activation propene activation step reveals that the component most sensitive to catalyst composition is the ligand-to-metal charge transfer energy, which is described by the band-gap. In combination with experimental work, we also show that when the band gap falls below 2.1 eV, the selectivity to acrolein rapidly declines because the surface oxygen atoms of the catalyst becomes become sufficiently active to oxidize the allyl alkoxide, the intermediate to acrolein, to CO and CO_2.

Finally, we have demonstrated that the role of Bi^{3+} cations in bismuth molybdate catalysts used for propene oxidation and ammoxidation derived from its ability to adsorb propene near Mo═O groups involved in the abstraction of a hydrogen atom from the methyl group of adsorbed propene and stabilizing the resulting Mo—OH group. Of the Mo-containing oxides examined, the strongest adsorption of propene occurs over Bi^{3+} cations that are present at the surface of $Bi_2Mo_3O_{12}$. To achieve a low reaction barrier for hydrogen atom abstraction the adsorbed propene must be proximate to a surface oxygen atom that has a low hydrogen adsorption energy (HAE). The latter property requires a highly-coordinated molybdenum atom at the oxide surface. We find that an oxygen atom *trans* to the oxo group to which a hydrogen is added increases the energy of the highest occupied molecular orbital, thereby reducing the energy required to rehybridize the molybdenum oxygen double bond from the singlet state to the triplet state. While molybdenum atoms that are greater than four-coordinate are disfavored energetically, they are needed to achieve a low HAE. Hence, the introduction of asymmetric Bi^{3+} in the surface layer of the parent structure and vacancies one layer below the surface give the mixed metal oxide the conformational flexibility to achieve favorable, higher molybdenum coordination after hydrogen addition.

Declaration of Competing Interest

The authors declare that they have no known competing financial interests or personal relationships that could have appeared to influence the work reported in this paper.

Acknowledgements

Funding for this work was provided by the Director, Office of Science, Office of Basic Energy Sciences, and by the Division of Chemical Sciences, Geosciences, and Biosciences of the U.S. Department of Energy at Lawrence Berkeley National Laboratory under Contract No. DE-AC02-05CH11231. Calculations presented in this work were conducted at the National Energy Research Scientific Computing Center (NERSC), which is supported by the Office of Basic Science of the U.S. Department of Energy under Contract No. DE-AC02-05CH11231.

Recommended articles Citing articles (0)

References

[1] R.K. Grasselli
Top. Catal., 21 (2002), pp. 79-88
CrossRef View Record in Scopus

[2] D. Arntz, A. Fischer, M. Höpp, S. Jacobi, J. Sauer, T. Ohara, T. Sato, N. Shimizu, H. Schwind
Ullmann's Encyclopedia of Industrial Chemistry
Wiley-VCH, Weinheim, Germany (2012)
Google Scholar

[3] J.F. Brazdil
Ullmann's Encyclopedia of Industrial Chemistry
Wiley-VCH, Weinheim, Germany (2012)
Google Scholar

[4] R.K. Grasselli, M.A. Tenhover, Ammoxidation, in: G. Ertl, H. Knözinger, F. Schüth, J. Weitkamp (Eds.), Handbook of Heterogeneous Catalysis, 2nd ed., 2008, p. 3489.
Google Scholar

[5] R.K. Grasselli
Catal. Today, 238 (2014), pp. 10-27
Article Download PDF View Record in Scopus

[6] J.F. Brazdil, J.F. Scheelite
Catal. Sci. Technol., 5 (2015), pp. 3452-3458
CrossRef View Record in Scopus

[7] R.K. Grasselli, J.D. Burrington, J.F. Brazdil
Faraday Discuss. Chem. Soc., 72 (1981), pp. 203-223
View Record in Scopus

[8] I. Matsuura, R. Schut, K.J. Hirakawa

Catal., 63 (1980), pp. 152-166
Article Download PDF View Record in Scopus

[9] P. Sprenger, W. Kleist, J.-D. Grunwaldt
ACS Catal., 7 (2017), pp. 5628-5642
CrossRef View Record in Scopus

[10] C.R. Adams, T.J. Jennings
J. Catal., 2 (1963), pp. 63-68
Article Download PDF View Record in Scopus

[11] C.R. Adams, T.J. Jennings
J. Catal., 3 (1964), pp. 549-558
Article Download PDF View Record in Scopus

[12] L.D. Krenze, G.W. Keulks
J. Catal., 61 (1980), pp. 316-325

[13] R.K. Graselli, J.D. Burrington
Ind. Eng. Chem. Prod. Res. Dev., 23 (1984), pp. 393-404

[14] A.K. Rappe
Mol. Phys., 102 (2004), pp. 289-299
View Record in Scopus

[15] J.D. Burrington, C.T. Kartisek, R.K. Grasselli
J. Org. Chem., 46 (1981), pp. 1877-1882
CrossRef View Record in Scopus

[16] W. M. H. Sachtler, N. K. DeBoer, in: Proceedings 3rd International Congress on Catalysis, Vol. 1, 1965, p 252.
Google Scholar

[17] Y. Zhao, D.G. Truhlar
J. Chem. Phys., 125 (2006), pp. 194101-194118
CrossRef View Record in Scopus

[18] C.C. McCain, G. Gough, G.W. Godin
Nature, 198 (1963), p. 989
CrossRef View Record in Scopus

[19] J.D. Burrington, C.T. Kartisek, R.K. Grasselli
J. Org. Chem., 46 (1981), pp. 1877-1882
CrossRef View Record in Scopus

[20] (a) A. Ayame, K. Uchida, M. Iwataya, M. Miyamoto
Appl. Catal., A, 227 (2002), pp. 7-17
Article Download PDF View Record in Scopus

(b) Z. Zhai, A. Getsoian, A.T. Bell
J. Catal., 308 (2013), pp. 25-36
Article Download PDF View Record in Scopus

[21] W. Ueda, K. Asakawa, C.-L. Chen, Y. Moro-Oka, T. Ikawa
J. Catal., 101 (1986), pp. 360-368
Article Download PDF View Record in Scopus

[22] G.W. Keulks
J. Catal., 19 (1970), pp. 232-235
Article Download PDF View Record in Scopus

[23] T.P. Snyder, C.G. Hill
Cat. Rev., 31 (1989), pp. 43-95
CrossRef View Record in Scopus

[24] C.R. Adams, H.H. Voge, C.Z. Morgan, W.E. Armstrong
J. Catal., 3 (1964), pp. 379-386
Article Download PDF View Record in Scopus

[25] G.W. Keulks, L.D. Krenze, Proceedings 6th International Congress on Catalysis p. 806 (1976).
Google Scholar

[26] J.L. Callahan, R.K. Grasselli, E.C. Milberger, H.A. Strecker
Ing. Eng. Chem. Prod. Res. Dev., 2 (1970), pp. 134-142
CrossRef View Record in Scopus

[27] I.K. Kolchin, S.S. Bobkov, L. Ya Margolia
Neftekhimiya, 4 (1964), pp. 301-307

[28] R.D. Wragg, P.G. Ashmore, J.A. Hockey
J. Catal., 31 (1973), pp. 293-303
Article Download PDF View Record in Scopus

[29] K. Aykan
J. Catal., 12 (1968), pp. 281-290
Article Download PDF View Record in Scopus

[30] J.D. Burrington, C.T. Kartisek, R.K. Grasselli

J. Catal., 66 (1980), pp. 347-367

[31] J. N. Allison, W. A. Goddard III in: Solid State Chemistry in Catalysis, American Chemical Society Symposium Series No. 279; Eds R. K Grasselli and J. F. Brazdil, 1985, pp. 23–36.
Google Scholar

[32] Y.H. Jang, W.A. Goddard III
Top. Catal., 15 (2001), pp. 273-289
CrossRef View Record in Scopus

[33] Y.H. Jang, W.A. Goddard III
J. Phys. Chem. B, 106 (2002), pp. 5997-6013
View Record in Scopus

[34] W.A. Goddard III, A. van Duin, K. Chenoweth, M.-J. Cheng, S. Pudar, J. Oxgaard, B. Merinov, Y.H. Jang, P. Persson
Top. Catal., 38 (2006), pp. 93-103
View Record in Scopus

[35] S. Pudar, J. Oxgaard, K. Chenoweth, A.C.T. van Duin, W.A. Goddard III
J. Phys. Chem. C, 111 (2007), pp. 16405-16415
CrossRef View Record in Scopus

[36] W.A. Goddard III, K. Chenoweth, S. Pudar, A.C.T. van Duin, M.-J. Cheng
Top. Catal., 50 (2008), pp. 2-18
CrossRef View Record in Scopus

[37] S. Pudar, J. Oxgaard, W.A. Goddard III
J. Phys. Chem. C, 114 (2010), pp. 15678-15694
CrossRef View Record in Scopus

[38] S. Pudar, W.A. Goddard III
J. Phys. Chem. C, 119 (2015), pp. 27370-27381
CrossRef View Record in Scopus

[39] Y. Du, A.L. Rheingold, E.A. Maatta
J. Am. Chem. Soc., 114 (1992), pp. 345-346
CrossRef View Record in Scopus

[40] H.H. Fox, K.B. Yap, J. Robbins, S. Cai, R.R. Schrock
Inorg. Chem., 31 (1992), pp. 2287-2289
CrossRef View Record in Scopus

[41] G. Hogarth, I. Richards

Transition Met. Chem., 35 (2010), pp. 111-115
CrossRef View Record in Scopus

[42] A.B. Getsoian, A.T. Bell
J. Phys. Chem. C, 117 (2013), pp. 25562-25578
CrossRef View Record in Scopus

[43] J.P. Perdew, K. Burke, M. Ernzerhof
Phys. Rev. Lett., 77 (1996), pp. 3865-3868
CrossRef View Record in Scopus

[44] B. Hammer, L.B. Hansen, J.K. Nørskov
Phys. Rev. B, 59 (1999), pp. 7413-7421
View Record in Scopus

[45] Y. Zhao, D.G. Truhlar
J. Chem. Phys, 125 (2006), Article 194101
CrossRef View Record in Scopus

[46] Y. Zhao, D.G. Truhlar
Theor. Chem. Acc., 120 (2008), pp. 215-241
CrossRef View Record in Scopus

[47] J. Paier, M. Marsman, K. Hummer, G. Kresse, I. C. Gerber, J, G. Ángyán, J. Chem. Phys., 125 (2006) 249901
Google Scholar

[48] J. Heyd, G.E. Scuseria, M. Ernzerhof
J. Chem. Phys., 118 (2003), p. 8207
CrossRef View Record in Scopus

[49] S.L. Dudarev, G.A. Botton, S.Y. Savrasov, C.J. Humphreys, A.P. Sutton
Phys. Rev. B, 57 (1998), pp. 1505-1509
CrossRef View Record in Scopus

[50] G. Kresse, J. Furthmüller
Phys. Rev. B, 54 (1996), p. 11169
CrossRef View Record in Scopus

[51] P.E. Blochl
Phys. Rev. B, 50 (1994), p. 17953
CrossRef View Record in Scopus

[52] G. Kresse, D. Joubert

Phys. Rev. B, 59 (1999), p. 1758
View Record in Scopus

[53] J. Sun, M. Marsman, G.I. Csonka, A. Pruzsinszky, P. Hao, Y.-S. Kim, G. Kresse, J.P. Perdew
Phys. Rev. B, 84 (2011), Article 035117
CrossRef View Record in Scopus

[54] R.B. Licht, A.T. Bell
ACS Catal., 7 (2017), pp. 161-176
CrossRef View Record in Scopus

[55] A. B. Getsoian, V. Shapovalov, A. T. Bell, J. Phys. Chem. C, 117 (20137123–7137.
Google Scholar

[56] J.D. Burrington, C.T. Kartisek, R.K. Grasselli
J. Catal., 81 (1983), pp. 489-498
Article Download PDF View Record in Scopus

[57] L. Stradella, G.Z. Vogliolo
Phys. Chem., 137 (1973), pp. 99-110
View Record in Scopus

[58] G.W. Keulks, L.D. Krenzke, T.M. Notermann
Adv. Catal., 27 (1979), pp. 183-225
Article Download PDF View Record in Scopus

[59] R.B. Licht, D. Vogt, A.T. Bell
J. Catal., 339 (2016), pp. 228-241
Article Download PDF View Record in Scopus

[60] A.B. Getsoian, Z. Zhai, A.T. Bell
J. Am. Chem. Soc., 136 (2014), pp. 13684-13697
CrossRef View Record in Scopus

[61] Comprehensive Handbook of Chemical Bond Energies; Ed. Y. R. Luo, CRC Press: Boca Raton, FL, 2003, p. 26.
Google Scholar

[62] B. Ruscic, A.F. Wagner, L.B. Barding, R.L. Asher, D. Feller, D.A. Dixon, K.A. Peterson, Y. Song, X. Qian, C.-Y. Ng, J. Liu, W. Chen, D.W. Schwenke
J. Phys. Chem. A, 106 (2002), p. 2727
View Record in Scopus

[63]

Note that because the electron assigned to the metal center in the •M—O• excited state enters the conduction band and becomes spatially delocalized over the crystal lattice, there is essentially zero exchange coupling between the metal-centered and oxygen-centered electrons in the excited state. The excited state energy is therefore independent of the net spin configuration (singlet or triplet). However, the DFT calculation on the •M—O• state is substantially more straightforward in the spin triplet case, so for convenience, excited states with triplet spin configurations were used in calculation of Ehyb.
Google Scholar

[64] Z. Zhai, M. Wütschert, R.B. Licht, A.T. Bell
Catal. Today, 261 (2016), pp. 146-153
Article Download PDF View Record in Scopus

[65] P. Sprenger, M. Stehele, A. Caur, A.M. Gänzler, D. Gashnikova, W. Kleist, J.-D. Grunwaldt
ACS Catal., 8 (2018), pp. 6462-6475
CrossRef View Record in Scopus

[66] L. Bui, R. Chakrabarti, A. Bhan
ACS Catal., 6 (2016), pp. 6567-6580
CrossRef View Record in Scopus

[67] R.B. Licht, A.B. Getsoian, A.T. Bell
J. Phys. Chem. C, 120 (2016), pp. 29233-29247
CrossRef View Record in Scopus

View Abstract